geosciences

MDPI

Article

Stress–Strain Investigation of the Rock Mass Based on Overcoring with CSIRO HI Cell Test and Numerical Modeling: A Case Study from an Italian Underground Marble Quarry

Riccardo Salvini [1,*], Andrea Ermini [1], Vivien De Lucia [1], Luisa Beltramone [1], Daniele Silvestri [1], Andrea Rindinella [1,*], Stefano Guido [2], Daria Marchetti [3] and Domenico Gullì [3]

[1] Department of Environment, Earth and Physical Sciences and Centre of Geotechnologies CGT, University of Siena, Via Vetri Vecchi 34, 52027 San Giovanni Valdarno, Italy
[2] SIAL.TEC Engineering S.R.L., Via San Giuseppe 24, 24060 Bergamo, Italy
[3] UOC Ingegneria Mineraria—USL Toscana Nord-Ovest, Tuscany Region, Piazza Sacco e Vanzetti, 54033 Carrara, Italy
* Correspondence: riccardo.salvini@unisi.it (R.S.); rindinella@unisi.it (A.R.)

Abstract: The present research illustrates the application of a methodological approach to studying the stress–strain distribution in a marble quarry of the Apuan Alps mining area (Italy). This study has been carried out in the framework of a project involving the University of Siena and the UOC Ingegneria Mineraria—USL Toscana Nord-Ovest, Tuscany Region. This stress–strain analysis aims foremost to monitor the slope stability conditions to guarantee a safe workplace for the personnel involved in mining activities, and to enable more sustainable long-term planning for excavation and production. The involved survey activities are as follows: (i) terrestrial laser scanning; (ii) engineering–geological data mapping; and (iii) in situ marble stress measuring through four CSIRO-type cell tests executed in different locations and at various depths within the underground excavation walls. The gathered data converged into numerical models of the quarry, both in 2D (DEM) and 3D (FEM), calibrated by in situ stress results through a rigorous back analysis assessment using least squares procedures. The created models represent a valuable tool for the identification and securing of risk areas and for future excavation planning in respect of the site efficiency and safety.

Keywords: CSIRO HI cell test; underground quarrying; stress–strain measuring; laser scanning; DEM and FEM numerical modeling; slope stability analysis; Apuan Alps

Citation: Salvini, R.; Ermini, A.; De Lucia, V.; Beltramone, L.; Silvestri, D.; Rindinella, A.; Guido, S.; Marchetti, D.; Gullì, D. Stress–Strain Investigation of the Rock Mass Based on Overcoring with CSIRO HI Cell Test and Numerical Modeling: A Case Study from an Italian Underground Marble Quarry. *Geosciences* **2022**, *12*, 441. https://doi.org/10.3390/geosciences12120441

Academic Editors: Elisabetta Cattoni, Gessica Umili, Roberto Valentino, Evelina Volpe and Jesus Martinez-Frias

Received: 21 October 2022
Accepted: 23 November 2022
Published: 30 November 2022

1. Introduction

Marble exploitation in the Apuan Alps (north-western Tuscany, Italy), performed since the Roman age, has highlighted, in the last decades, a delicate balance between the high demand of the international market, high production costs, workers' safety, and environmental sustainability. The increase in the excavation rate due to the most modern techniques (line drilling and sawing) to produce large rectangular blocks needs safety requirements to be satisfied without reducing the yield. Monitoring of the slope stability conditions is useful to guarantee a safe workplace for the personnel involved in mining activities and to enable a more sustainable long-term planning for excavation and production.

A quantitative description of rock discontinuities is crucial to understand the stability conditions of a rock mass. The mechanical behavior of marble rock mass depends on the combined effect of several factors related to geo-structural conditions (discontinuity and excavation geometry) and in situ stress. An engineering–geological survey provides parameters to characterize the nature of the discontinuities (orientation, spacing, persistence, surface roughness, etc.).

Slope 3D models, based on high-resolution point cloud data, can be produced using several techniques, such as total station (TS) [1], terrestrial laser scanning (TLS) [2–4], airborne light detection and ranging (LiDAR) [5,6], unmanned aerial vehicle (UAV) photogrammetry [5,7,8], and UAV LiDAR [9–11].

The most adopted procedures in slope stability analysis are the kinematic and limit equilibrium methods. The kinematic method is based on the evaluation of possible instabilities and failures generated by the presence of discontinuities in the rock mass. This method could be used as a rapid evaluation of key blocks generating potential failures [12,13]. The limit equilibrium method is based on defining the potential mechanism of failure and is based also on the acting forces and the related factor of safety (FS) in a particular geomechanical condition both in 2D and 3D [14]. Both methods are suitable for simple geometry issues, but not for more complex ones.

To analyze complex potential instability scenarios, the use of numerical modeling, such as the distinct element method (DEM) [15] or the finite element method (FEM) [16], should be considered. The main difference between them is how the medium is considered, as the DEM method is used for discontinuous mediums, while the FEM is for continuous ones. Software based on DEM, such as UDEC (universal distinct element code by ITASCA©) and 3DEC (three-dimensional version of UDEC, ITASCA©), are meant for various complex slope conditions in different environments [17–19]. Similarly, among the available software to be used in the FEM analysis, RS2 by Rocscience© [20], and the related 3D RS3 version [21,22], can also be cited.

The FS is a useful index to determine how close a slope is to failure, and how much its accuracy is consistent with that of geotechnical input data. The geotechnical and geomechanical properties of the materials used in numerical modeling can be defined through laboratory tests and, partially, by engineering–geological surveys. For instance, in the case of rocky materials the use of tests, such as point load, uniaxial and triaxial compression, as well as the direct and indirect determination of the tensile and shear strengths, is useful for establishing the material properties to be inserted in the model. Similarly, there are in situ tests to be used for determining the physical and mechanical properties of rock and the structural fabric of the rock mass, defined by systems of structural discontinuities (e.g., bedding surfaces, joints). Engineering properties of fractured rock masses, such as strength and permeability, are strictly dependent on the nature of their structural fabric.

Another important input for studying slope stability is the in situ stress state. The in situ stress, in rocky material, can be measured through "overcoring tests" (a type of stress relaxation test) with the 2D doorstopper method [23] and the 3D CSIRO (Commonwealth Scientific and Industrial Research Organization) cells method [24]. These tests are suitable for monitoring short-term stress changes following the cell installation and allow the acquisition of response curves (strain, temperature, and overcoring depth in relation to time) before, during, and after overcoring. Moreover, the CSIRO cell method allows the definition of the 3D local stress and the computation of the rock elastic constants [25,26]. Several authors used the CSIRO cell method to determine the elastic parameters of rocks. Ouanas et al. [27], for example, applied this method in the southern border of the French Massif Central to define the elastic parameters of Tournemire argillite. Krietsch et al. [28] measured the in situ stress of crystalline rocks at the Grimsel Test Site (Switzerland) and compared the results from overcoring, hydraulic fracturing and induced seismicity. In other cases, the CSIRO cell method was used for studying the in situ stress and the related slope stability in quarries and mines [29–32] and for monitoring the stress changes in the excavation of tunnels [33,34] and radioactive wastes [35].

This paper aims to deal with rock mass stability analysis to support the design and safety controls of an underground marble quarry. The stability analysis is supported by the identification and quantitative assessment of intact rock and discontinuity properties. In situ surveys were carried out to collect the engineering–geological properties, stress conditions, and geometric setting of the rock mass bounding an underground quarry of the

Apuan Alps. Finally, two numerical modeling approaches (DEM, FEM) were performed to estimate the stress distribution through the rock mass facing the marble excavation areas.

2. Geological Setting

The quarry under study, known as "Sottovettolina", is located in the Municipality of Massa (Italy). It belongs to the Apuan Alps, a metamorphic complex composed of two major units, the Massa unit and the Apuan unit (Figure 1). The Apuan Alps are the largest tectonic window in the inner Northern Apennines where deep levels of the belt are exposed [36,37].

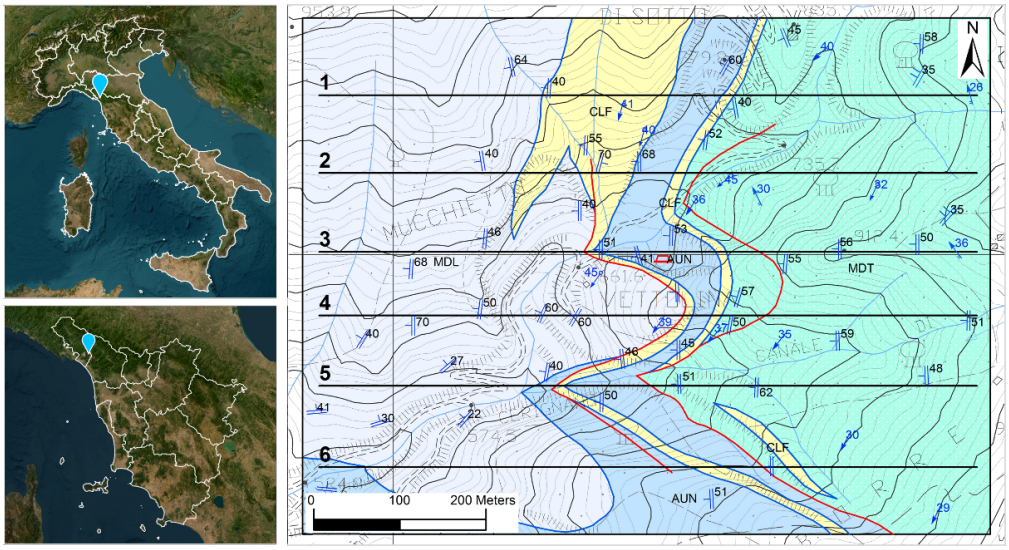

Figure 1. Geological map of the Sottovettolina quarry and surrounding area (**right**). Map legend is as follows: MDL—dolomitic marble; AUN—marble; CLF—cherty meta-limestone; MDT—radiolarian chert. The red symbol shows the quarry location. Red lines indicate tectonic boundaries of secondary importance. Black lines indicate the six traces of the geological sections used for the 3D modeling of the quarry area. Sketch maps in the left side show the location of the study area in Italy (light blue pin).

The stratigraphy of the area consists of a Paleozoic basement overlain unconformably by Upper Triassic–Oligocene meta-sediments. Thin Triassic continental to shallow water Verrucano-like deposits represent the Mesozoic cover, and they are followed by Upper Triassic–Liassic carbonate platform meta-sediments including dolomites, dolomitic marbles, and marbles. These are overlain by Upper Liassic–Lower Cretaceous cherty meta-limestone, cherts, and calcschists, and by Lower Cretaceous–Lower Oligocene sericitic phyllites, and calcschists, with marble interlayers, which are related to deep-water sedimentation during drowning of the former carbonate platform. The sedimentary history of the domain is completed by the Oligocene sedimentation of turbiditic sandstones, known as "Pseudo-macigno" [38].

The Apuan Alps result from two main tectono-metamorphic events (D1 and D2 phases [36]) which summarize the progressive deformation of the Adriatic continental margin during the continental subduction and the subsequent exhumation [39]. The tertiary continental collision between the Sardinia–Corsica block and the Adria plate caused the ductile compressional event D1, while the following D2 extensional event led to an isostatic rebalance [36]. During the D1 event, the stacking of the tectonics unit belonging to the Tuscan and Ligurian domains occurred, and a progressive deformation developed in two stages. The main of these phases is represented by isoclinal micro- to kilo-metric scale folds whose axial plane is characterized by a greenschist foliation. This foliation, which distinguishes most of the metamorphic rocks of the Apuan Alps, is associated with a stretching lineation SW-NE trending, interpreted as the main transport direction of the inner Northern Apennines [37,40]. The structures were reworked during the D2 event

when different generations of folds and locally high strain zones, associated with the exhumation and vertical shearing, developed [41]. The result of the second deformative phase is a complex mega-antiform with a NW–SE Apenninic trending axis. It is with this this trend that non-cylindrical parasitic folds with sub-horizontal axial planar crenulations are associated. The direction of transportation is toward the east, on the eastern limb of the antiform, and toward the west on the western side. Brittle structures (low-angle, high-angle faults, and joint systems) characterize the late stages of D2. These structures are correlated to the final exhumation and uplift of the metamorphic units in a frame of late- to post-orogenic regional extension of the inner part of the Northern Apennines [42].

Molli et al. [43], Fellin et al. [44] and references therein say that the peak of metamorphism occurred in the early Miocene (at approximately 27 My [45]), during the early D1 phase, at temperatures around 350–450 °C and pressure approximately 0.6 GPa. During the early stage of the D2 phase, the metamorphism took place at a temperature above 250 °C. According to zircon fission-track ages, the structures associated with this last phase were dated between 11 and 8 My [44].

In this context, the Sottovettolina quarry develops underground on the left bank of the Cerignano canal at an altitude of 660 m a.s.l. The marbles in this area belong to the core of a minor isoclinal anticline belonging to the inverted limb of the "Orto di Donna—Mt Altissimo" D1 syncline. In this area, the structures associated with the D1 event are characterized, at all scales, by a main axial plane foliation having an approximately NS direction, immersion towards the west, and an average dip of about 50°. In the proximity of the quarry, evidence of ductile structures associated with the D2 event have not been identified, except at the scale of the outcrop. In the western area of the geological map (Figure 1) the main foliation shows a dip direction rotation and a decrease in the dip value; this variation can be associated with the M. Rasori fold related to the D2 extensional event. Nevertheless, the latter structure does not affect the geometry of the marble in the Sottovettolina quarry, which can be associated with a simple monocline structure dipping towards the west.

The marketable marble varieties extractable from the quarry are the "Calacatta Luccicoso" and the "Grigio Forno", belonging to the groups of veined marble and grey marble, respectively [46]. Veined marble is a meta-limestone that is variable in color from pearl-white to very light gray, often containing some dense dark gray veins due to the presence of pyrite. Locally, there are dolomitic levels with gray-yellowish cherts. Figure 2 shows the geological cross section referred to as trace Nr. 3 of Figure 1.

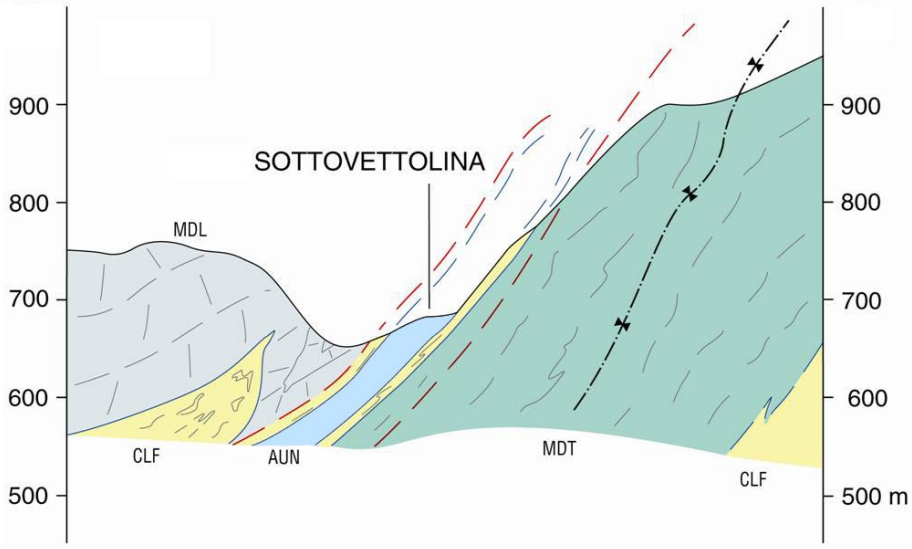

Figure 2. Geological cross-section of the Sottovettolina quarry and surrounding area (Map legend is as follows: MDL—dolomitic marble; AUN—marble; CLF—cherty meta-limestone; MDT—radiolarian chert). The geological cross-section is referred to as Nr. 3 of Figure 1.

3. Materials and Methods

3.1. In Situ Survey

The geometry of the Sottovettolina quarry through TLS, the geological setting, and the engineering–geological characteristics of the rock mass were collected by in situ surveys to address modeling for slope stability analysis. The estimation of in situ stresses was computed by CSIRO hollow inclusion (HI) cell tests.

Output from these surveys provided the input data to be utilized in modeling the quarry conditions through DEM and FEM approaches with the goal of assessing the rock mass stability.

3.1.1. Engineering–Geological Survey

A detailed engineering–geological survey was carried out inside the quarry and surrounding areas by Pandolfi Engineering s.r.l. [47]. The available data has allowed us to improve our knowledge of the geological setting of the area in relation to the main characteristics of bedding, foliation, stretching lineations, joints, and the fold axis. Every discontinuity was described in terms of dip, dip direction, spacing, length, persistence, termination, aperture, infill, weathering, humidity, JRC (joint roughness coefficient [48]) and JCS (joint wall compressive strength [49]), as estimated using the Barton comb and the Schmidt hammer rebound, respectively.

Some properties of the joints were used in modeling (only within the marble) and assigned to the surfaces representing the lithological boundaries between marble and cherty meta-limestones, and between the latter and radiolarian cherts. The choice of using only discontinuities within the marble, and not the ones in other lithologies, is based on the hypothesis that the latter have a negligible impact on the stability of excavation areas due to their distance from the quarry fronts. Data from the engineering–geological survey is shown later in the text, in the Results chapter.

3.1.2. Terrestrial Laser Scanning

Point Cloud Acquisition

The use of TLS, based on the time of flight elapsed by a laser pulse along precise directions, allowed us to collect 3D dense point clouds of the area morphology. The surface was detected by measuring the distance from the instrument using the speed of the light and the time that an impulse takes to reach a surface and to be reflected along its path [50]. The TLS survey was carried out by employing a Trimble© TX8 device (Figure 3) that allows us to set the spot spacing and duration of every single scan. A scan time of 10 min and a spacing of 5.7 mm at 30 m were chosen for a 360° wide scanning view. The high reflectivity of the quarry walls due to their bright color and low roughness provides a high-intensity return signal, related to a few tens of meters away from the origin of the laser scanner, leading to high spatial density [51].

The quarry is characterized by a single chamber with a total length of about 110 m and a height of just over 50 m. The TLS survey required six scans to cover the whole surface of the quarry and to guarantee a sufficient overlap among them. The number of scans was chosen as a balance between minimizing possible occlusions and shadows in the output, and the amount of data to be processed. The data output of every scan is a 3D high-density point cloud, in which every point is defined by cartesian coordinates (X, Y, Z) relative to the scanner location and orientation.

Figure 3. Trimble© TX8 laser scanner during setting up of data acquisition.

Coregistration of all the point clouds was performed using the iterative closest point (ICP) algorithm to obtain a unique 3D model of the quarry (Figure 4). The cartesian coordinates of the TLS survey were framed by a topographic survey in an absolute reference system using optical targets placed in specific positions within the excavation area and its surroundings (see next Paragraph).

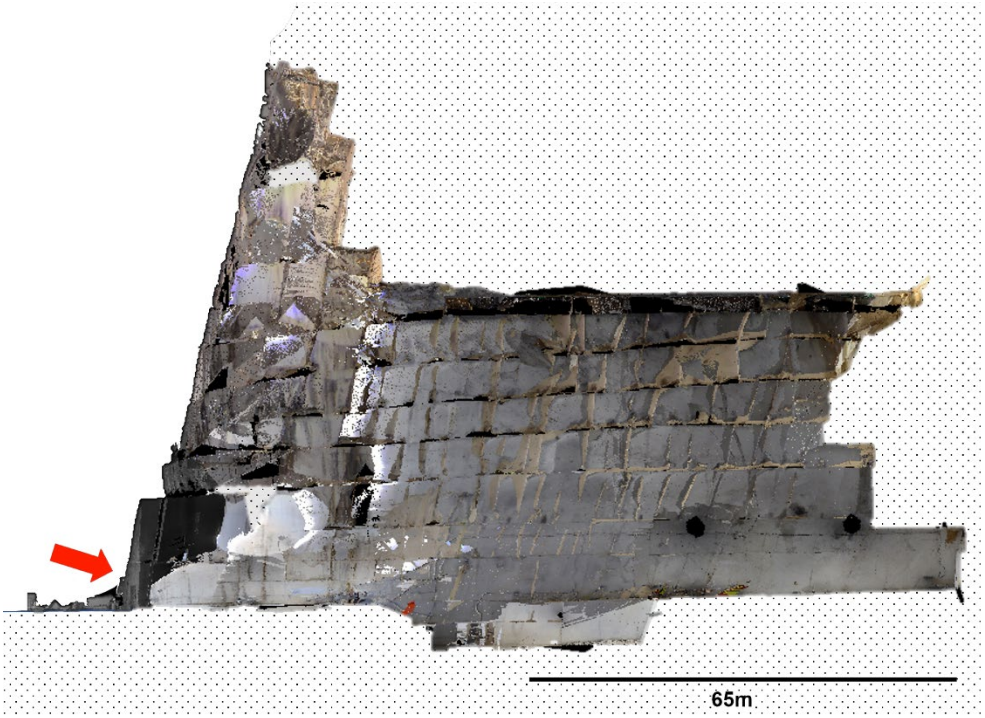

Figure 4. Union of all the 3D point clouds after the coregistration process. The red arrow indicates the quarry entrance. Perspective view; the scale bar is indicative only.

Topographic Survey and Point Cloud Georeferencing

The topographic survey, the aim of which was geolocating the 3D model of the quarry area, was carried out using a total station (TS) model Leica© MS50 (Figure 5A). The cartesian coordinates of a series of fixed and removable optical targets (Figure 5B and 5C), placed in specific positions inside and outside the underground quarry, were determined by measuring their angular and distance with respect to the origin of the local reference system. The coordinates of each target were framed within the geodetic reference system UTM ETRF2000 Zone 32N thanks to the presence of fixed optical targets at the entrance and inside the quarry, located in positions with known coordinates derived from GNSS surveys (global navigation satellite system) carried out by the personnel of the Center of Geotechnologies in previous years. The measurement of the fixed optical targets was used for the orientation and georeferencing of the entire project. The positions of the movable targets have been chosen to have a minimum of three targets visible in every single scan acquired by TLS.

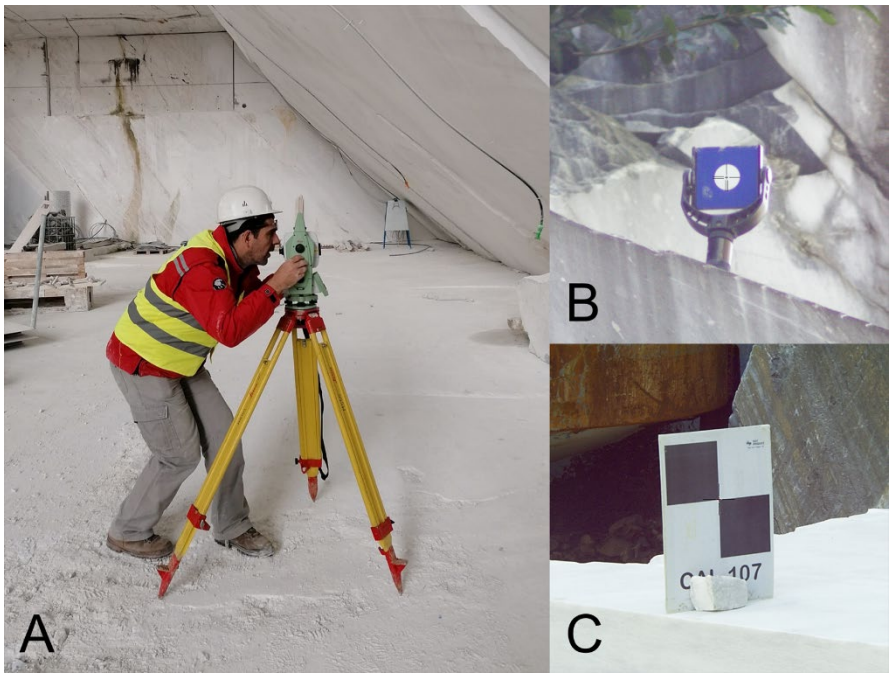

Figure 5. Leica© MS50 Total Station (**A**); detail of a fixed optical target (**B**); removable optical target (**C**).

The advantage of integrating topographic surveys and TLS is that it reduces the effect of error propagation from the first scan position; in fact, the accuracy of the registration process, and subsequently of the georeferencing, depends on the topographic survey [52,53]. The TS instruments, which provide millimetric accuracy [54–58], are increasingly used in different civil engineering sectors, such as mining [59].

The surveyor defined the local reference system by choosing the origin of a cartesian axis (set as 0,0,0 coordinates) and defining its orientation, referred to as 0-azimuth direction, using one fixed optical target measured by TS. The survey was initialized by measuring all targets visible in the first scan. Additional targets, necessary to register all the scans, were collected using the inverse intersection method by moving the TS to different positions within the quarry during the ongoing survey. By this method, the subsequent TS positions were estimated using a minimum of three points with known coordinates. Using this technique, the coordinates of 21 targets in the local reference system were collected. The topographic data were processed by the Leica© Infinity software, to transform the local coordinates of all targets to the UTM ETRF2000 Zone 32N reference system. This operation was carried out by using the known absolute coordinates of the fixed targets and roto-translating the whole targets set. Finally, the six point clouds were coregistered and georeferenced.

3.1.3. In Situ Stress Tests

The CSIRO HI cell is currently one of the most widely used methods for measuring the in situ rock stress and the estimation of the elastic parameters thanks to the overcoring method [24]. Here, a CSIRO triaxial HI cell is equipped with 12 strain gauges plus a thermistor for measuring the hole inner temperature. The test requires the drilling of a first hole, 164 mm in diameter, up to a planned depth (Figure 6A); then, a second pilot hole with a smaller diameter (i.e., 38 mm) is made up at the bottom of the hole, coaxial with the previous one. After carefully cleaning and drying the hole walls, the cell is cemented inside it by gluing it with a specific resin that allows the strain gauges to become part of the rock in about 18 h (glue setting times). Subsequently, after recording the strain gauge deformations in real-time, the overcoring of the rock volume containing the cell is carried out; this is set up on the largest diameter hole [60]. Then, deformations are triggered by the detensioning that is developed when the specimen is separated from the rock. Thus, all the electrical signals, detected by measuring the HI cell during the various stages of the test, can be continuously collected. At the end of the overcoring, a biaxial compression test, using the Hoek–Franklin pressure cell (Figure 6D), is performed on the rock specimen and a stress–strain graph is created. The method allows also for the determination of the rock elastic parameters (Young's modulus, E; Poisson's ratio, ν). It is noted that this test should have been carried out as soon as possible after the overcoring, while the rock retains its in situ moisture content [27].

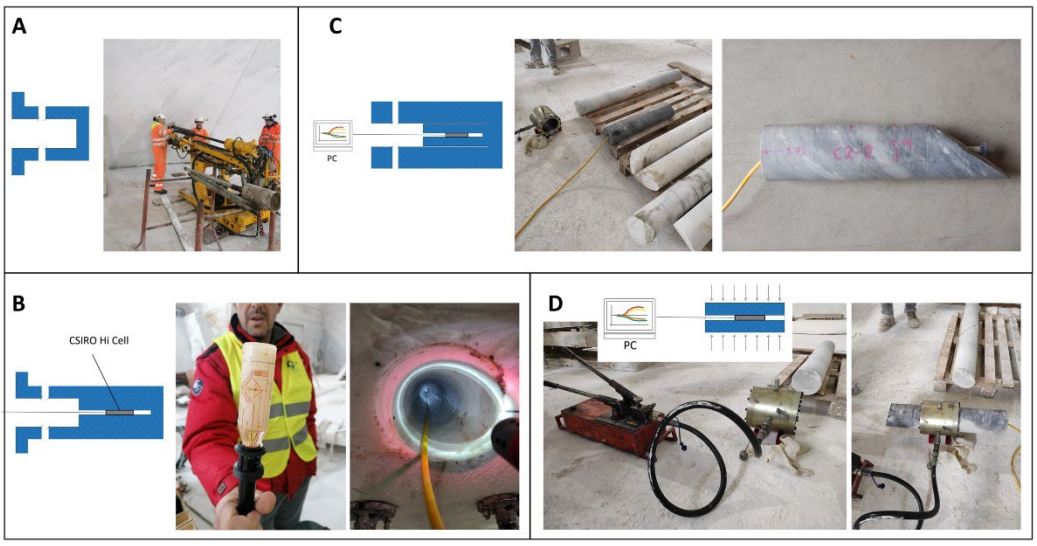

Figure 6. Summary of the working phases using the CSIRO HI cell and overcoring method. (**A**) Drilling of the first borehole up to the planned depth; (**B**) mounting of CSIRO HI cell inside the pilot borehole; (**C**) cell overcoring; (**D**) execution of biaxial compression test through the Hoek–Franklin cell and stress–strain data estimation.

In this study, the stress measurements were based on four overcored CSIRO HI cells placed in two sub-horizontal boreholes, referred to as C1 and C2 in Figure 7. The boreholes have been carried out on the western wall of the quarry's chamber, orthogonally oriented with respect to the quarry front. The CSIRO HI cells, named C 1-1, C 1-2, C 2-1, and C 2-2 in Figure 7, are equipped with two axial (A0, C0), five tangential (A90, B90, C90, E90, F90) and five +45° (A45, B45, B135, C45, D135) inclined strain gauges, plus a thermistor. They were installed at different depths to provide a punctual measurement of the rock's three-dimensional tension state.

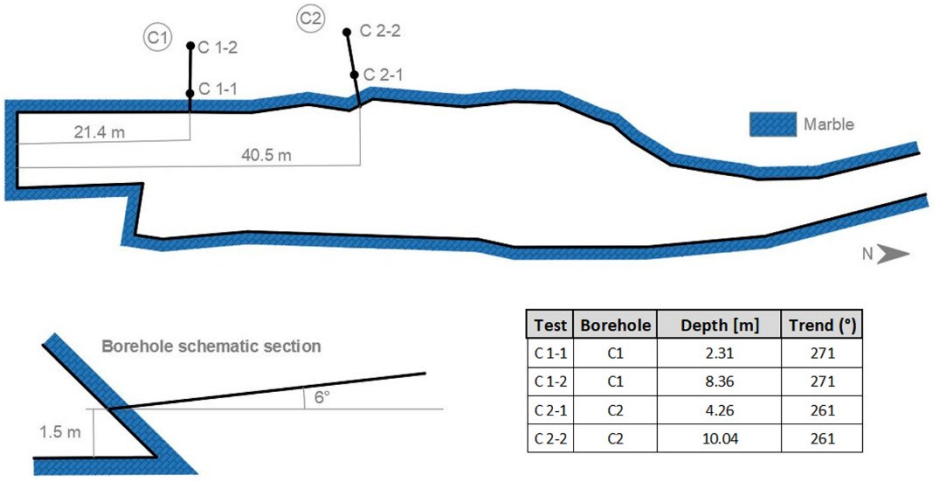

Test	Borehole	Depth [m]	Trend (°)
C 1-1	C1	2.31	271
C 1-2	C1	8.36	271
C 2-1	C2	4.26	261
C 2-2	C2	10.04	261

Figure 7. Planimetric view of the Sottovettolina quarry, location of the in situ stress measurements (C 1-1, C 1-2, C 2-1, and C 2-2), and exemplificative schematic section aimed at showing the borehole dip. The table on the right resumes the geometry of the tests.

The output data provides, for each CSIRO HI cell, a real-time graph showing the trend of deformations [micro-strain, $\mu\varepsilon$] versus the depth [cm]. Deformation data was corrected for temperature variation according to the C method [61] proposed by TRT (Top Rock Technologies).

The relationship between the strain gauge deformations and the radial pressure comes from the linear solution proposed by [62,63], where the basic assumptions of the interpretative model are as follows: (i) homogeneous and linearly elastic rock; (ii) infinite outer diameter; (iii) infinite drill length and infinite rock extension; (iv) uniform tensional state around the test. As the radial pressure generates an effect equivalent to that of an isotropic natural stress state, by measuring the variation of the radial pressure P and using $\{\Delta\varepsilon\}$ the vector of the corresponding strain variations as previously measured by the strain gauges, it is possible to use the following equation:

$$\{\Delta\varepsilon\} = P\ \{H\} \quad (1)$$

where $\{H\}$ is a column matrix function of (i) angular position, dip, and length of the strain gauges of the CSIRO HI cell; (ii) internal diameter of the inclusion (cell and glue layer); (iii) elastic characteristics of the inclusion; (iv) diameter of the pilot hole and the core instrumented with the cell; (v) angles representing the orientation of the borehole in the global reference system XYZ (X = east, Y = north, Z = vertical); (vi) Young's modulus (E) and Poisson's ratio (ν) of the rock. As $\{H\}$ is a non-linear function of the rock's unknown elastic constants, the Equation (1) defines a certain system of non-linear indirect observations with only two unknown variables, E and ν, solved by a multiple non-linear regression analysis.

Once the elastic parameters have been estimated, the natural in situ stress state is derived from the following equation proposed by [62,63]:

$$\{\Delta\varepsilon\} = -[W]\ \{\sigma_{xyz}\} \quad (2)$$

where $\{\sigma_{xyz}\}$ is the column matrix containing the six components of the stress tensor in the XYZ global system (σ_{xx}, σ_{yy}, σ_{zz}, τ_{yz}, τ_{xz}, and τ_{xy}) and $[W]$ is the column matrix conceptually analogous to the previous $\{H\}$ matrix of Equation (1). Equation (2) represents a determined system of homogeneous linear equations in six unknowns. The solution of the system which can be solved by using a multiple linear regression analysis provided the average natural stress state existing in the rock volume object of the measurement.

The in situ stress tensor $\{\sigma_{xyz}\}$ was calculated for each CSIRO HI cell according to the global reference XYZ system. The values are provided by SIAL.TEC Engineering s.r.l. (responsible for the CSIRO HI cell tests) with a confidence limit of 68% referred to the stan-

dard deviation. In the radial compression tests, it was assumed that the measured strains are independent gaussian random variables, with a mean value equal to the observed one and standard deviation corresponding to that of the regression residuals, as follows:

- $\Delta i = \Delta\varepsilon i.computed - \Delta\varepsilon i.observed$ residual corresponding to the i-th observation;
- $\sigma\varepsilon = \Sigma\Delta i2/(N - 2)$ standard deviation of the residuals.

Ten thousand random extractions from the N distributions of the test data were simulated, generating a sample of 10,000 pairs of "E, ν" parameters whose analysis provides the confidence limits of Young's modulus and the Poisson's ratio. Values obtained were used to perform the calibration of the stress state in numerical modeling, as described in the next paragraphs.

3.2. Rock Slope Stability Analysis

3.2.1. Finite Element Method in RS3©

Model Creation

The RS3 (Rocscience©) finite element analysis software is designed for the 3D analysis of geotechnical structures for civil and mining applications, and it allows us to automate slope stability assessment through the reduction in the mechanical strength [20]. Modeling with the finite element method (FEM) develops systems of algebraic equations that approximate solutions for partial differential equations. This computation is performed by breaking down a problem domain into smaller and simpler components, i.e., the elements. The FEM begins with the definition of the domain and geometry of the model, defining the materials and their properties. Then, the stress state is set, and the boundary conditions are defined in terms of forces and displacements (along the X, Y, and Z axes). In the next phase, the model is discretized by creating meshes (in computer graphics, a collection of vertices, edges, and faces that defines the shape of a polyhedral object) possibly customizing the density in the regions considered critical. Finally, the model is computed, and the obtained results are analyzed. This method involves the progressive reduction in the strength parameters until the analysis no longer reaches convergence; this is the limit equilibrium condition and the relationship between the starting value of the material strength parameters and the limit equilibrium value provides the overall FS of the analysis [64].

From the above description, inputs for the FEM analysis of underground excavations include the following parameters:

- Geometry, arrangement, and sequence of excavation;
- In situ stress state (main stress and orientation values);
- Strength and deformation characteristics of rock mass units and other large-scale geological structures.

The first step of the work carried out concerned the import of the geometries of the external morphology and the excavation area. The latter comes from the TLS survey, while for the surrounding external area the regional data from aerial LiDAR was used. Through the Agisoft Metashape© and Rhinoceros© software, the respective meshes were obtained and processed. Once inserted into the RS3© software, the meshes underwent, in addition to further topological corrections, a decimation, respectively, to about 3000 faces for the interior and 18,500 faces for the external area. This operation was necessary in order to use simplified geometries, reducing calculation times, while, at the same time, maintaining the fundamental geometries of the study area.

The geometry of the model (Figure 8), with overall dimensions of 700 × 500 × 300 m, takes the general shape of a box inside which the cavity has been excavated.

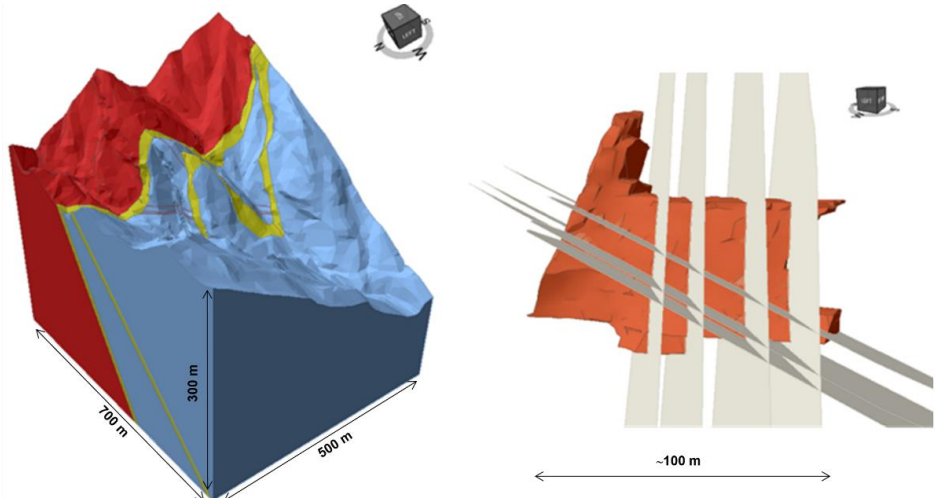

Figure 8. 3D geological model of the Sottovettolina quarry used in slope stability analysis (**left**); lithologies are indicated by colors, as follows: red = cherty meta-limestone; yellow = radiolarian chert; light blue = marble. Detail of discontinuity planes affecting the cultivation chamber (**right**). Perspective views; the scale bars are indicative only.

All the joint systems affecting the marble quarry were initially considered for the creation of the RS3© model; however, the reduced spacing of certain discontinuity sets means that the material is too fragmented. As a consequence, it was decided to consider only the discontinuities affecting the cavity with a higher spacing and which are visible on the quarry walls.

According to [65], the mechanical behavior of white marble of the Apuan Alps can be assumed as being linear elastic and isotropic. Hence, the Mohr–Coulomb model [66], which is the conventional model for elasto-plasticity in rock mechanics, was used for the intact rock, while joints were simulated with a Coulomb slip model [67].

The following steps are concerned with the definition of the model materials and properties, as well as the boundary conditions with constraints that limit the displacements in the chosen directions. Geotechnical properties of lithologies derived from the results of the CSIRO HI cell tests and from previous analyses presented in [47].

In this case study, the auto-restrain (surface) option was used to apply a 3D constraint to the model at the bottom and the inner boundary [20]. The upper surface and the natural slope, on the other hand, were left free from constraints. Then, the meshing procedure was performed in 3D using 10-noded tetrahedral elements.

Model Calibration

A calibrated model has been created thanks to a reiterate procedure, written using the MATLAB© language, which provides a multiple linear regression analysis (MLRA) of a system of overdetermined equations. The MLRA, based on Equation (3), is derived from the "superposition principle", according to which whenever a certain effect depends linearly on several independent causes, it results as the sum of the effects individually produced by each cause. Equation (3) is as follows:

$$\{\sigma\} = [A]\{\sum\} + \{\lambda\} \quad (3)$$

where σ are the on-site measurements from the CSIRO HI cells, A is the stress state in the borehole calculated by applying a unitary initial stress to the model, λ is the stress state calculated in the borehole by applying only the rock unit weight, and ∑ is the unknown uniform initial stress state of the model. By applying the stress values obtained from the linear regression results as the main stresses, 3D models were calibrated in RS3©.

3.2.2. Distinct Element Method in UDEC©

Model Creation

The Universal Distinct Element Code (UDEC, ITASCA©), based on the distinct element method (DEM), is a software used worldwide to analyze the stability conditions of natural and anthropic structures (slopes, dams, tunnels, excavations, etc.). The DEM, first introduced by [68], assumes rocky mass as an aggregation of discrete blocks and discontinuities as contact surfaces [15,69].

The presence of discontinuities within the rock mass leads to the assumption that the material can be considered a discontinuous medium [70]. This characteristic is the principal element that distinguishes it from a continuous medium, such as soil and isotropic materials.

The contact forces and displacements (rotation and complete detachments), generated at the interfaces between blocks, are calculated with tracing movements and new consecutive contacts [69]. The numerical representation of this dynamic behavior, made of a continuous generation of contacts, is represented by a time-stepping algorithm that assumes velocities and accelerations as constant during a timestep [70]. In other words, during a small-time step, perturbations cannot propagate to the neighboring elements. To calculate contact forces and trace block motion, respectively, force-displacement law is applied to all contacts, and Newton's second law is applied to all blocks. The following Figure 9 explains schematically how the calculation cycle in UDEC© works for rigid and deformable blocks.

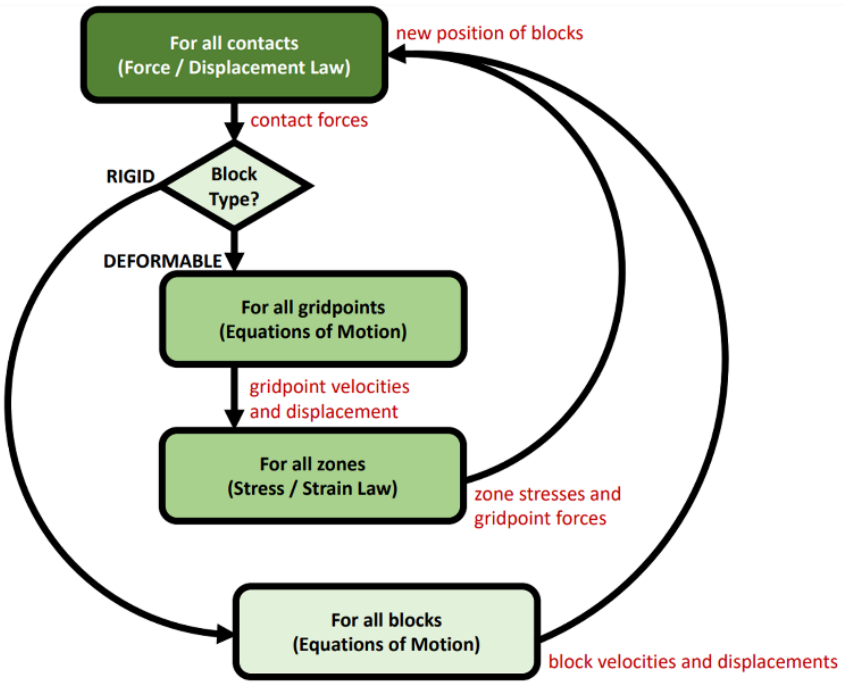

Figure 9. Schematic flow representing the numerical calculation steps in UDEC© (from [71]), adapted with permission from Ref. [71]. Itasca Consulting Group, Inc. (2014).

From the RS3© model, two sections in correspondence with the CSIRO HI cells boreholes were created. These planar vertical cross-sections were oriented respecting the directions of the boreholes and were named, respectively, S1 for borehole C1 and S2 for borehole C2 (Figure 10).

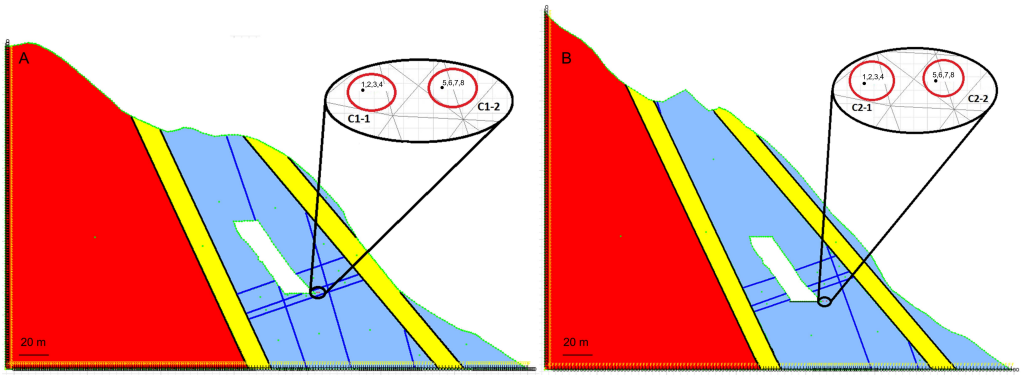

Figure 10. S1-C1 (**A**) and S2-C2 (**B**) cross-sections of the Sottovettolina underground marble quarry. Lithologies and discontinuities are indicated by colors, as follows: red = cherty meta-limestone; yellow = radiolarian chert; light blue = marble; black = lithological boundary; blue = marble discontinuity. The progressive numbers from 1 to 8 indicate the "histories" set in correspondence of the CSIRO HI cell tests aiming to monitor the xx, yy, xy, and zz stress tensor values.

The model blocks were considered deformable, and the assigned constitutive models were, respectively, the Mohr–Coulomb plasticity model [66] for lithologies, and the Coulomb slip model for discontinuities [67], in analogy to what had been established in the RS3© modeling. The same approach, described in Paragraph 3.2.1, was used for the discontinuities affecting the rock mass. Only the main discontinuities on the quarry walls were modeled in such a way to avoid that real spacing, derived from the engineering–geological surveys, would excessively fragment the model. The real spacing of joints would cause the material to behave as a continuous medium and, therefore, was not optimal for DEM analysis. Model boundaries were fixed by resetting the X and Y velocities along the bottom and the left model limit. Gravity was fixed at 9.81 m/s^2.

To trace the stress evolutions during the calculation, the function “history” was set in correspondence of the CSIRO HI cell measurements aiming to monitor the xx, yy, xy, and zz stress tensor values (Figure 10).

Before assessing the stability of the quarry fronts, the models were firstly solved to check their initial equilibrium with gravity as the only applied force.

Theoretically, the equilibrium ratio between the maximum unbalanced forces and the representative internal forces is considered to estimate the equilibrium of the rock mass [71] before, when the model is undisturbed, and after when the excavation progresses. When the equilibrium ratio reaches a value between 0.1% and 1%, the initial equilibrium can be considered satisfactory. Figure 11 shows both the models for the S1 and S2 sections reaching the equilibrium and satisfying the limit of 1×10^{-5} with a maximum number of cycles set to 100,000.

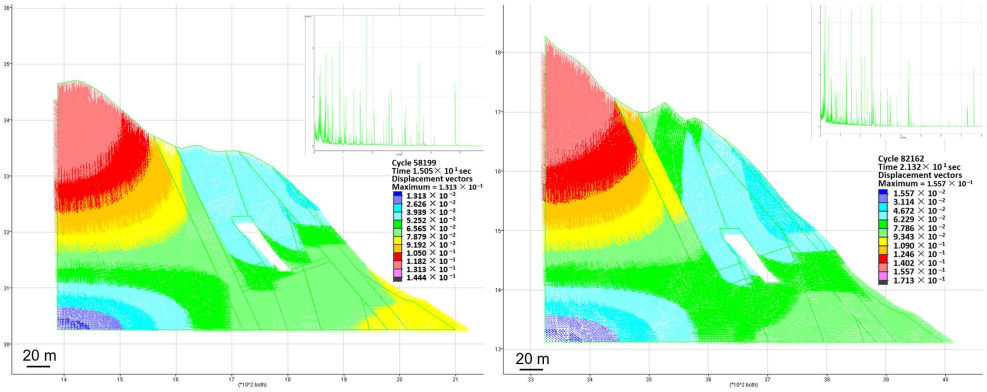

Figure 11. Model S1 (**left**) and model S2 (**right**) reaching the equilibrium condition.

Model Calibration

Similar to what was described for the three-dimensional RS3© model, in the two-dimensional case within UDEC©, the calibration procedure, still under the assumption of linear elastic material, follows Equation (3). In 2D, the main differences in computation are as follows: the lithostatic stress state {λ} calculated by the model at the test point has only 4 components; the matrix of coefficients [A] calculated by the model at the test points has dimension 4 × 4, and the model's unknown uniform initial stress state {∑} is a 4-component column matrix. For each test, the stress tensor {σ} was calculated from the measurement results by using the three-dimensional to two-dimensional transformation law according to the following equation:

$$\{\sigma_{2D}\} = [H]\ \{\sigma_{3D}\} \quad (4)$$

where [H] is the 4 × 6 rotation matrix which depends on the orientation of the analyzed section in respect to the geographic north. The procedure was applied to sections S1 and S2, and the residual values of the stress components at the test sites in the pre- and post-calibration model were computed.

4. Results

4.1. Engineering–Geological Data

Basing on data measured by Pandolfi Engineering s.r.l. [47] during the engineering–geological survey carried out inside the quarry and the surrounding areas, Table 1 reports in bold the six main joint sets affecting the marble lithology, described in terms of dip, dip direction, and spacing.

Table 1. Geometrical characteristics of joint systems [47].

Lithology	Joint System	Dip (°)	Dip Direction (°)	Spacing (m)
Marble	**K1**	**56**	**273**	**2–6**
Marble	**K2 (1.1)**	**83**	**331**	**6–10**
Marble	**K2 (1.2)**	**79**	**156**	**6–10**
Marble	**K2 (2)**	**86**	**12**	**6–10**
Marble	**K3**	**64**	**180**	**>10**
Marble	**K4**	**22**	**124**	**>10**
Radiolarian chert	J1	58	269	0.2–0.6
Radiolarian chert	J2	80	19	2–6
Radiolarian chert	J3	66	168	6–10
Radiolarian chert	J4	80	311	>10
Cherty meta-limestone	J1	60	269	0.6–2
Cherty meta-limestone	J2	68	146	6–10
Cherty meta-limestone	J3	77	22	6–10

Table 2 shows the mechanical properties of intact rock material, such as the unit weight, the rock elastic parameters (Young's modulus and Poisson's ratio), the peak cohesion, the peak friction angle, the peak tensile strength, the bulk modulus, and the shear modulus as derived from the stress tests of this work and data reported in [47].

Table 2. Engineering–geological characteristics of rock materials.

Lithology	Unit Weight (MN/m^3)	Poisson's Ratio	Young's Modulus (MPa)	Peak Cohesion (MPa)	Peak Friction Angle (°)	Peak Tensile Strength (MPa)	Bulk Modulus (MPa)	Shear Modulus (MPa)
Marble	0.0270	0.3	85,000	7.015	54.62	–3.432	94,444	31,500
Cherty meta-limestone	0.0256	0.3	18,500	1.626	53.81	–0.627	13,333	7115
Radiolarian chert	0.0264	0.3	16,000	1.745	56.17	–0.609	15,416	6153

Table 3 shows the properties of joints considered in modeling (only within the marble) and those assigned to the surfaces representing the lithological boundaries between marble and cherty meta-limestones and between the latter and radiolarian cherts.

Table 3. Engineering–geological properties of discontinuities.

	Joint Shear Stiffness (MPa/m)	Joint Normal Stiffness (MPa/m)	Peak Friction Angle (°)	Peak Cohesion (MPa)	Dilation Angle (°)
Joint in marble	10,000	40,000	35	0.05	5
Lithological boundary	2000	10,000	25	0.05	5

4.2. Point Cloud Coregistration and Georeferencing

The TS survey, aimed at estimating the coordinates of 21 targets in the local reference system and executed by the inverse intersection method, resulted in an error lower than 1 mm. The overall cloud-to-cloud error, resulting from the coregistration of the six point clouds, was equal to 3.6 mm, while the georeferencing error was 1.6 cm.

4.3. Data from In Situ Stress Tests

Data recorded by the CSIRO HI cells allowed us to compute the trend of deformations along the borehole depth for each test site. Figure 12 shows the real-time graphs of deformations [micro-strain, με] versus the depth [cm] as computed after the correction for temperature variation.

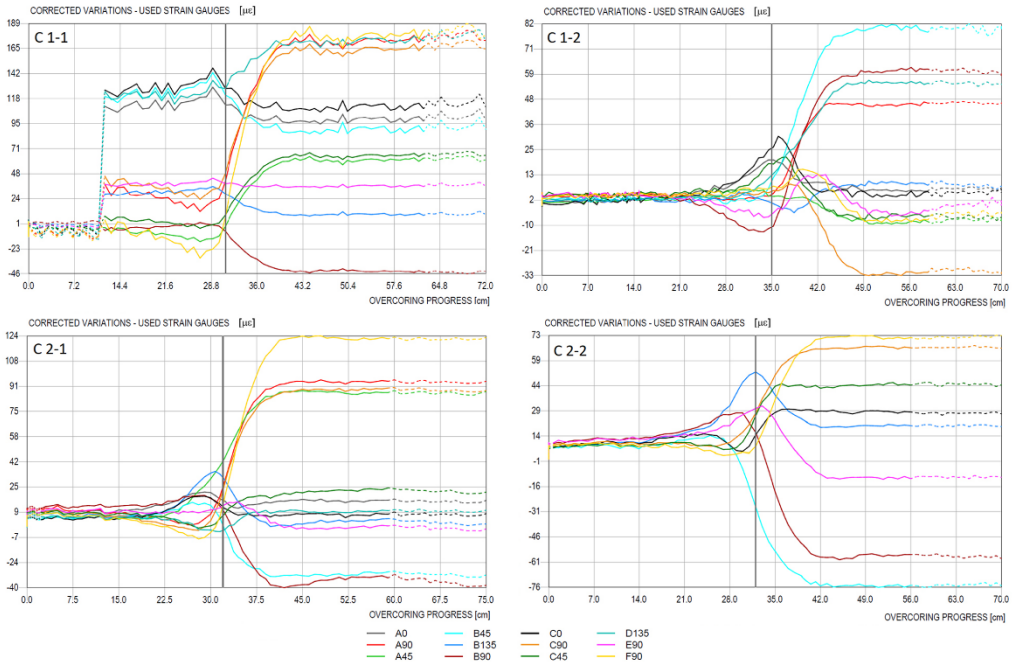

Figure 12. Graphs of the CSIRO HI cells correlating the deformations (με) registered by the 12 oriented strain gauges versus the borehole depth (cm).

Figure 13 shows the relationship between the strain gauge deformations and the radial pressure, as obtained by the biaxial tests carried out through the Hoek–Franklin pressure cell. Furthermore, in this case, deformation data was corrected for temperature variation according to the C method [61]. The trends of the stress–strain graphs shown in Figure 13 confirm the linear behavior as proposed by [62,63].

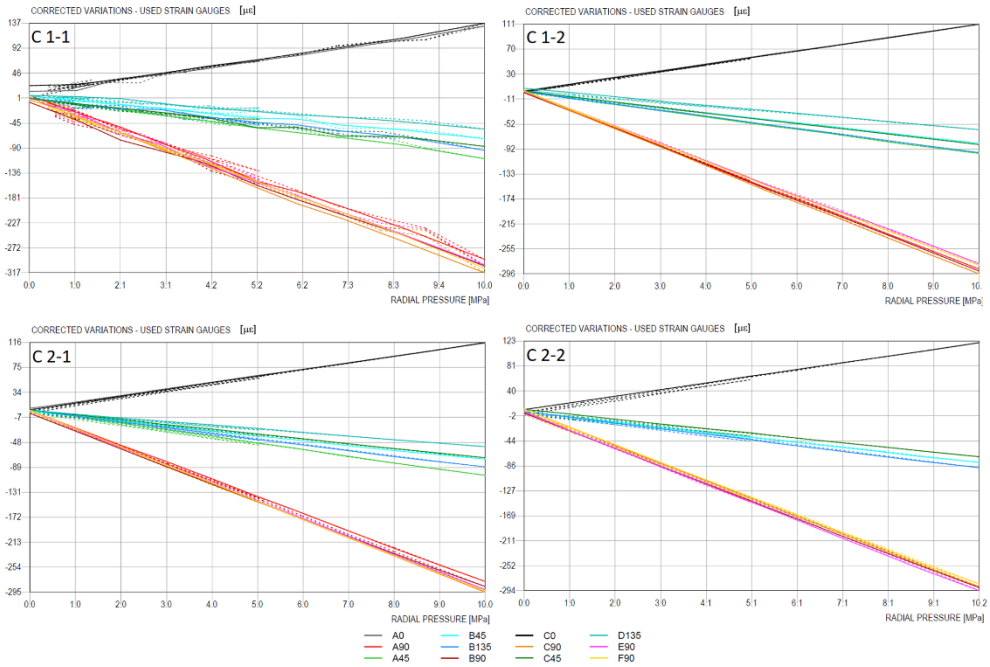

Figure 13. Stress–strain graphs of each specimen as obtained during the biaxial tests carried out through the Hoek–Franklin pressure cell. Deformation values (με), registered by each oriented strain gauge, are reported in the *y*-axis versus the radial pressure (Mpa) in the *x*-axis.

Table 4 shows the elastic parameters as computed from biaxial compression tests, while in Table 5, the in situ stress tensors $\{\sigma_{xyz}\}$, calculated for each CSIRO HI cell according to the global reference XYZ system, are shown.

Table 4. Elastic parameters derived from biaxial compression tests. Here, E = Young's modulus, ν = Poisson's ratio, C n-n = CSIRO HI cell at different depth.

	C 1-1	C 1-2	C 2-1	C 2-2
E [MPa]	87,673 ± 1872	89,127 ± 1330	88,488 ± 1846	88,276 ± 931
ν	0.37 ± 0.03	0.35 ± 0.02	0.36 ± 0.03	0.36 ± 0.02

Table 5. Calculated in situ stress tensors $\{\sigma_{xyz}\}$ for each CSIRO HI cell.

CSIRO HI Cell	σ_{xx} [MPa]	σ_{yy} [MPa]	σ_{zz} [MPa]	τ_{xy} [MPa]	τ_{xz} [MPa]	τ_{yz} [MPa]
C 1-1	0.44 ± 0.41	0.19 ± 0.16	5.15 ± 0.17	–0.24 ± 0.15	0.46 ± 0.10	0.20 ± 0.17
C 1-2	1.47 ± 0.24	1.86 ± 0.10	0.29 ± 0.10	0.97 ± 0.09	0.59 ± 0.06	0.88 ± 0.10
C 2-1	1.26 ± 0.28	–0.04 ± 0.12	3.72 ± 0.12	–0.49 ± 0.10	–0.88 ± 0.06	0.21 ± 0.12
C 2-2	0.86 ± 0.91	–0.80 ± 0.30	1.76 ± 0.39	–1.75 ± 0.25	–0.77 ± 0.23	–0.30 ± 0.46

4.4. RS3© Modeling

The deformation and stress states measured using the CSIRO HI cells method have shown that the material has a homogeneous, isotropic, and linear behavior. Then, the reiterate procedure, properly written using the MATLAB© language, was used to calibrate the RS3© model. In the graph of Figure 14, which compares the stress values measured by the CSIRO HI cells with those calculated by the model in the same positions after calibration, a good data correlation can be observed; the fitting coefficient of adjusted correlation (Ra) is equal to 0.721.

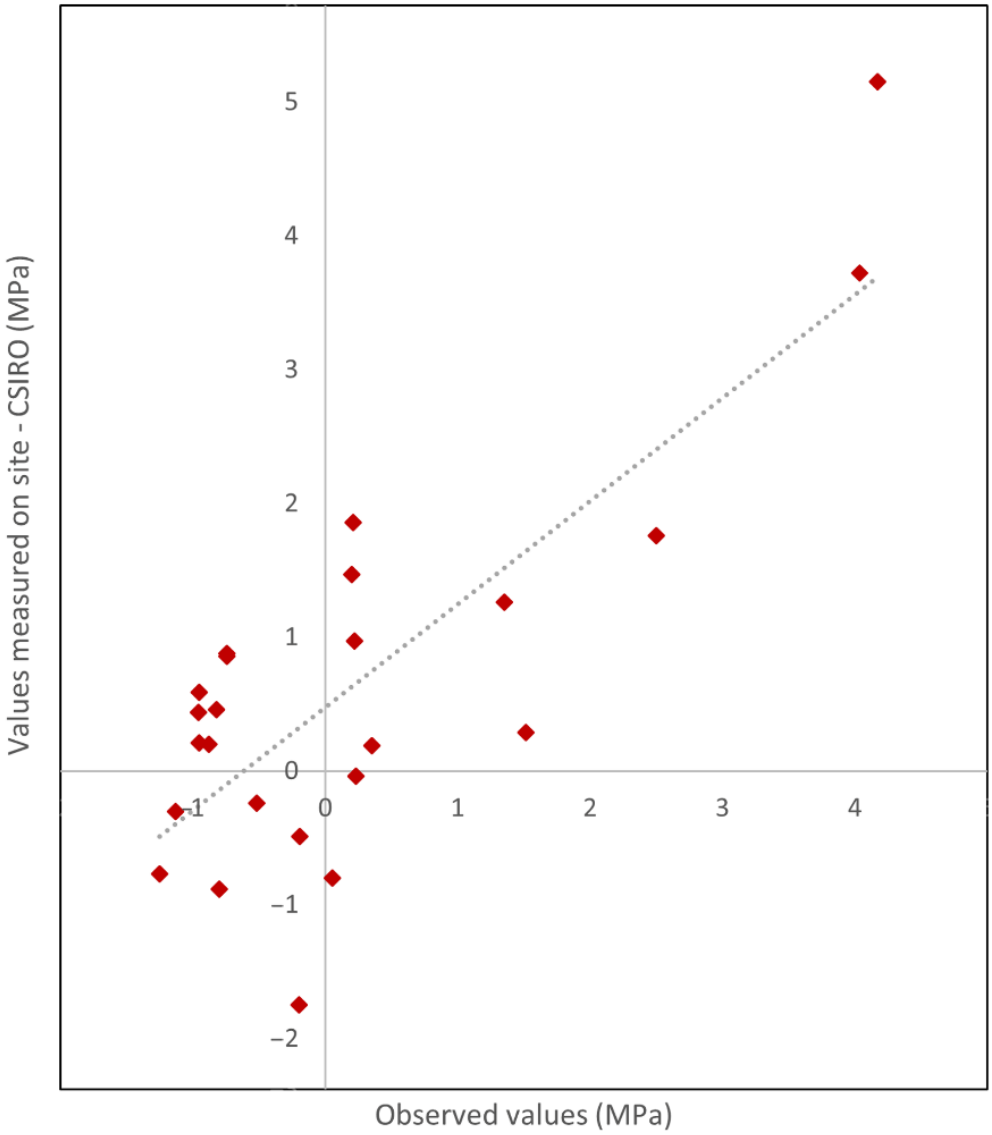

Figure 14. Correlation between the stress values observed in the CSIRO tests and those after model calibration in RS3©.

As further evidence of the accuracy of calibration, Figure 15 shows two graphs representing the trend of the three principal stresses (σ_1, σ_2, and σ_3), as measured using the in situ CSIRO HI cells and results after model calibration.

The calibration allowed us to obtain extensive information about the stress field acting on-site at the current condition of the quarry along the S1 and S2 sections (Figure 16), the relative displacements, the velocity, etc. As an example, Figures 17 and 18 show the deviatoric stress $\sigma_1-\sigma_3$, which can give an estimation of the rock mass strength.

Moreover, on the basis of the calibrated 3D model, it was possible to simulate the next excavation step of the zone currently under marble exploitation (colored in gray in Figure 19). In this way, the consequences of the stress field variations were assessed step-by-step as the excavation was progressing.

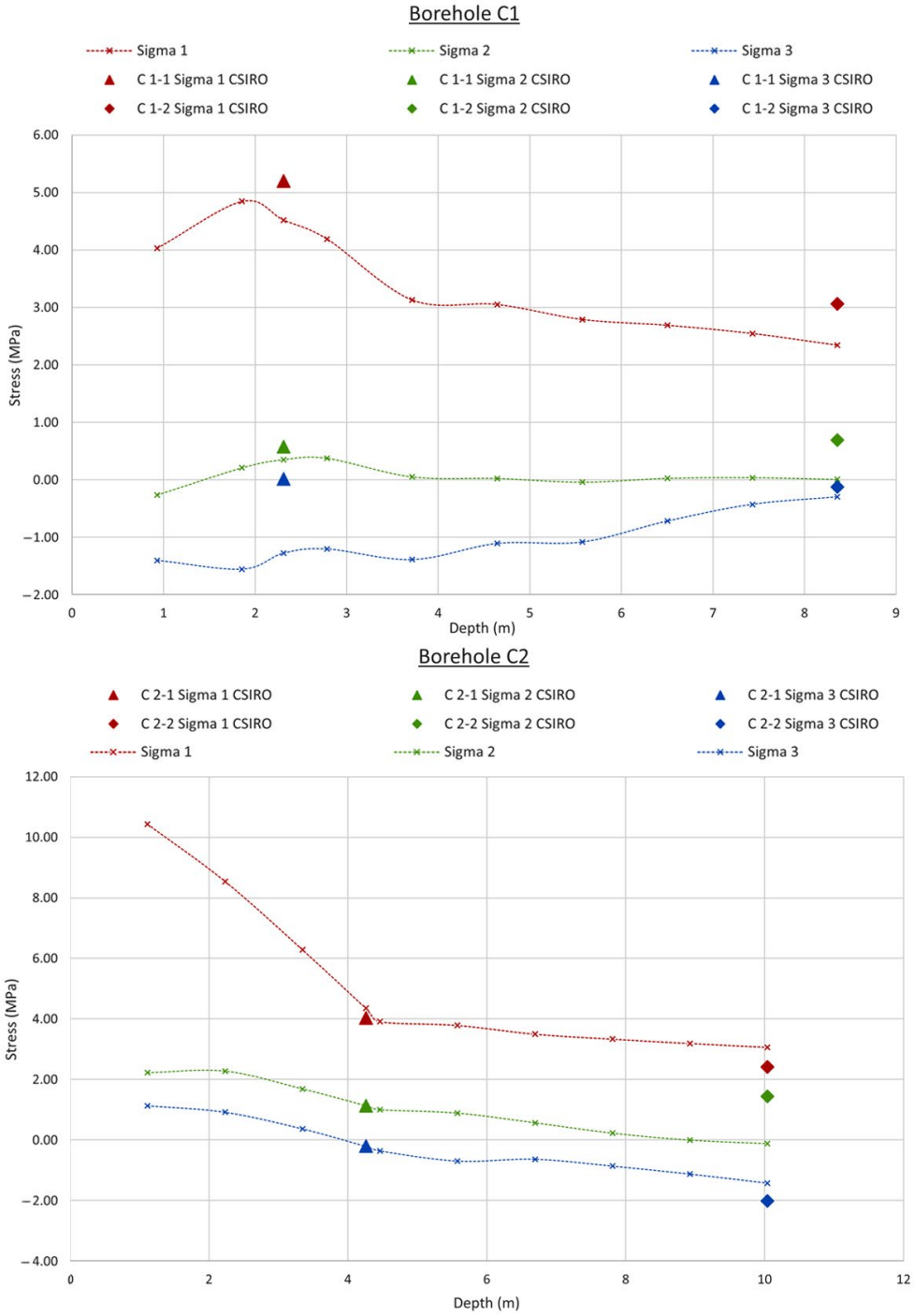

Figure 15. Trend of the principal stresses (σ_1, σ_2, and σ_3) versus the depth of C1 and C2 boreholes after model calibration (dotted lines) and their punctual values as obtained from the in situ CSIRO HI cell measurements (triangles and rhombuses).

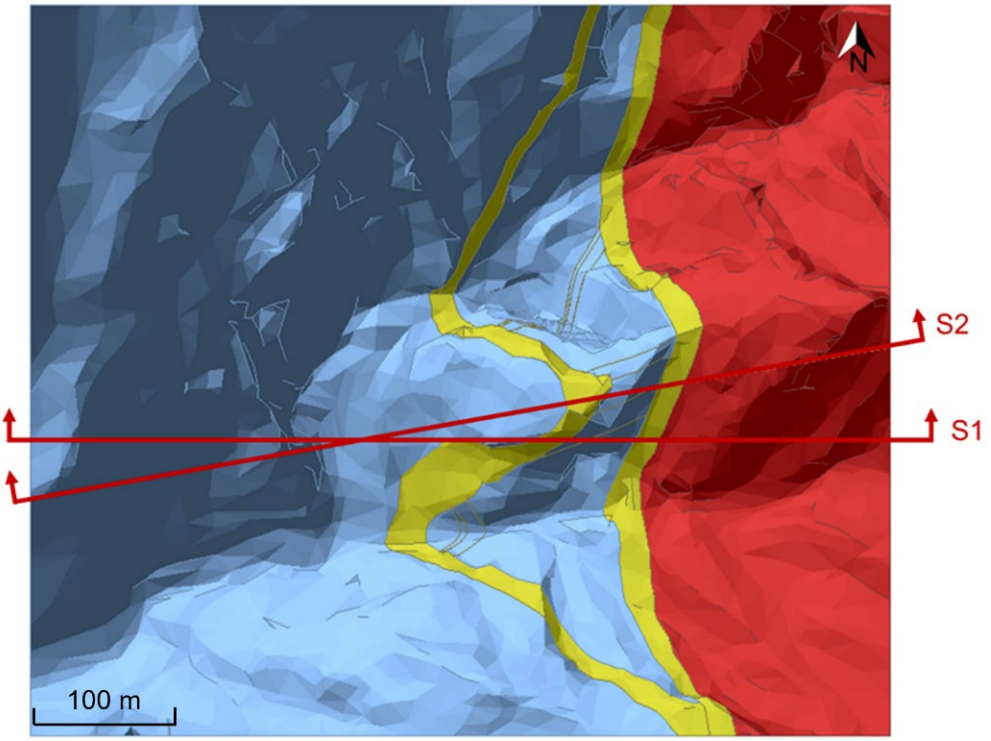

Figure 16. Planimetric view of the 3D geological model. The traces of sections S1 and S2 coinciding and oriented along the CSIRO test sites C1 and C2, respectively, are shown in red. The arrows indicate the look direction of Figure 17, Figure 18, Figure 20, and Figure 21.

Figure 17. Deviatoric stress (σ_1–σ_3) of Section S1 calculated in MPa.

Figures 20 and 21 show the deviatoric stress σ_1–σ_3 as computed, simulating the next excavation phase. The principal stresses around the quarry chamber present the following values: σ_1 ranges from a minimum of −3.5 MPa to a maximum of 32 MPa, σ_3 ranges from −21 MPa to 4 MPa, and the deviatoric stress shows a maximum value of 29 MPa.

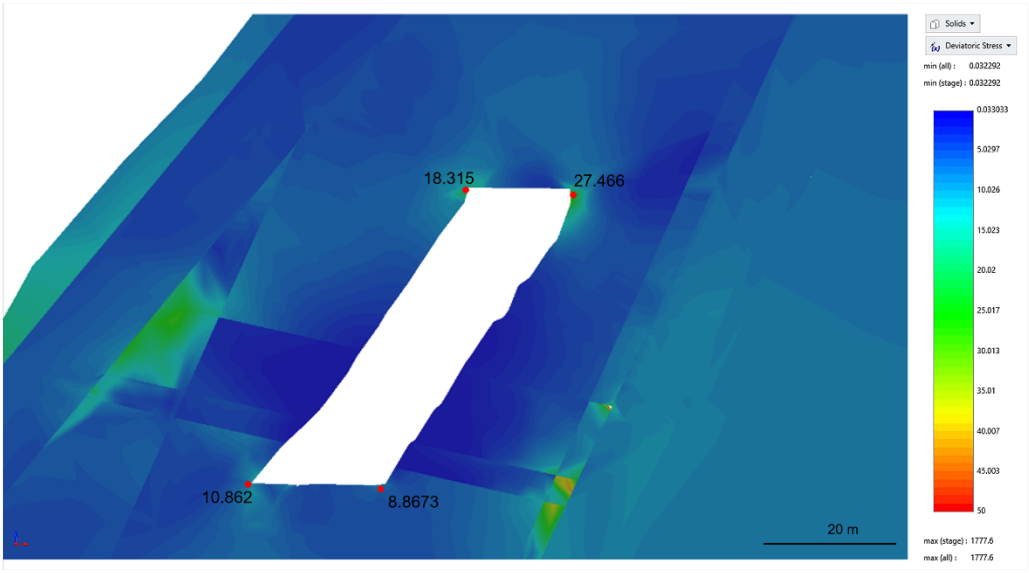

Figure 18. Deviatoric stress (σ_1–σ_3) of Section S2 calculated in MPa.

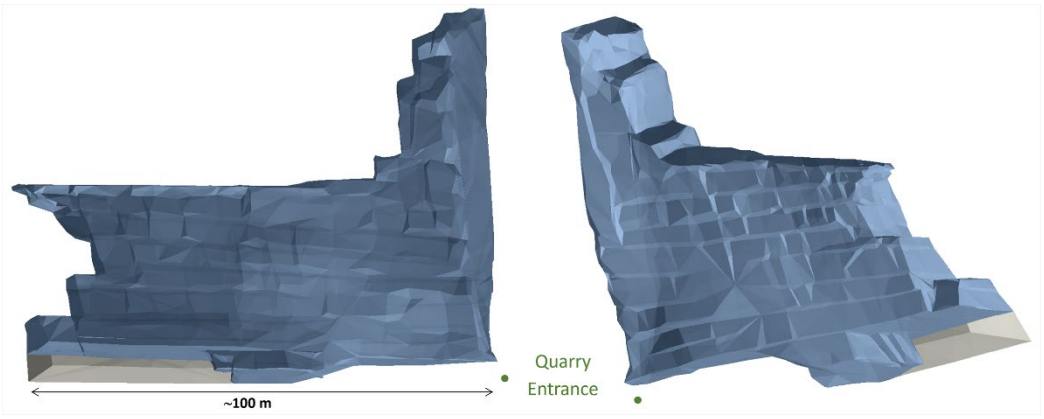

Figure 19. 3D model of the quarry inner part (blue) with the simulation of the excavation advancement (grey). Perspective views; the scale bar is indicative only.

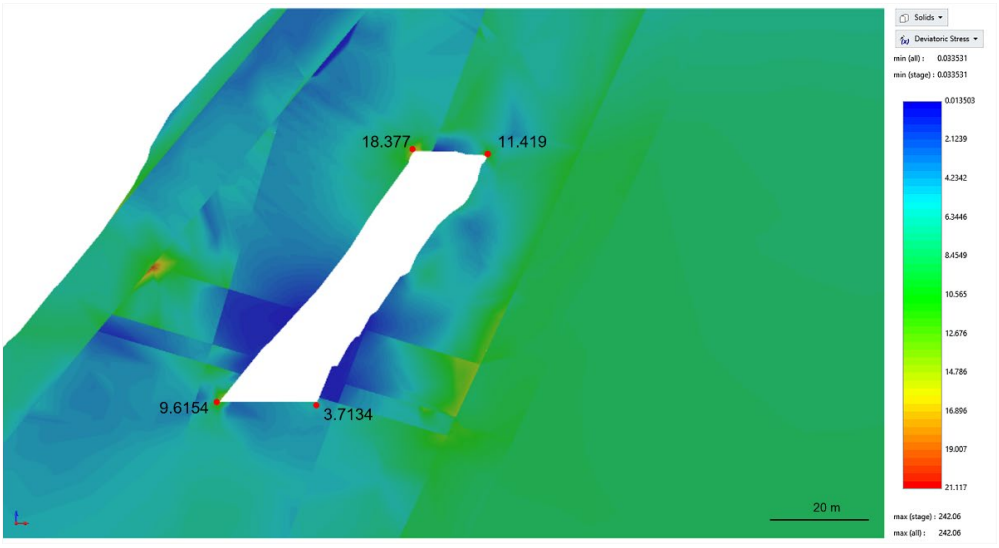

Figure 20. Deviatoric stress (σ_1–σ_3) of Section S1 calculated in MPa; the model includes the representation of future excavation.

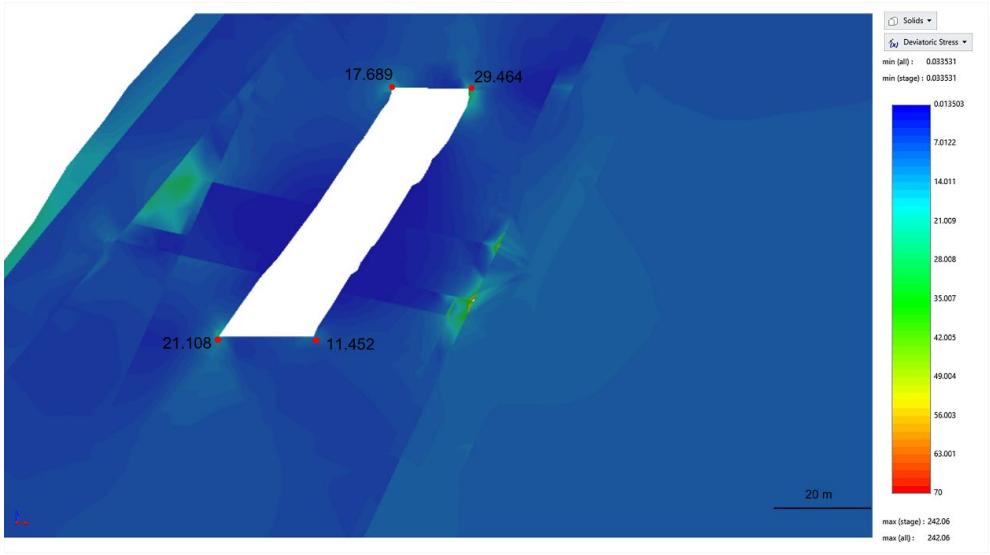

Figure 21. Deviatoric stress (σ_1–σ_3) of Section S2 calculated in MPa; the model includes the representation of future excavation.

4.5. UDEC© Modeling

The calibration procedure of the two-dimensional case within UDEC© was applied to sections S1 and S2, and the comparison among the residual values of the stress components at the test sites in the pre- and post-calibration model shows an evident improvement, as testified in Figure 22.

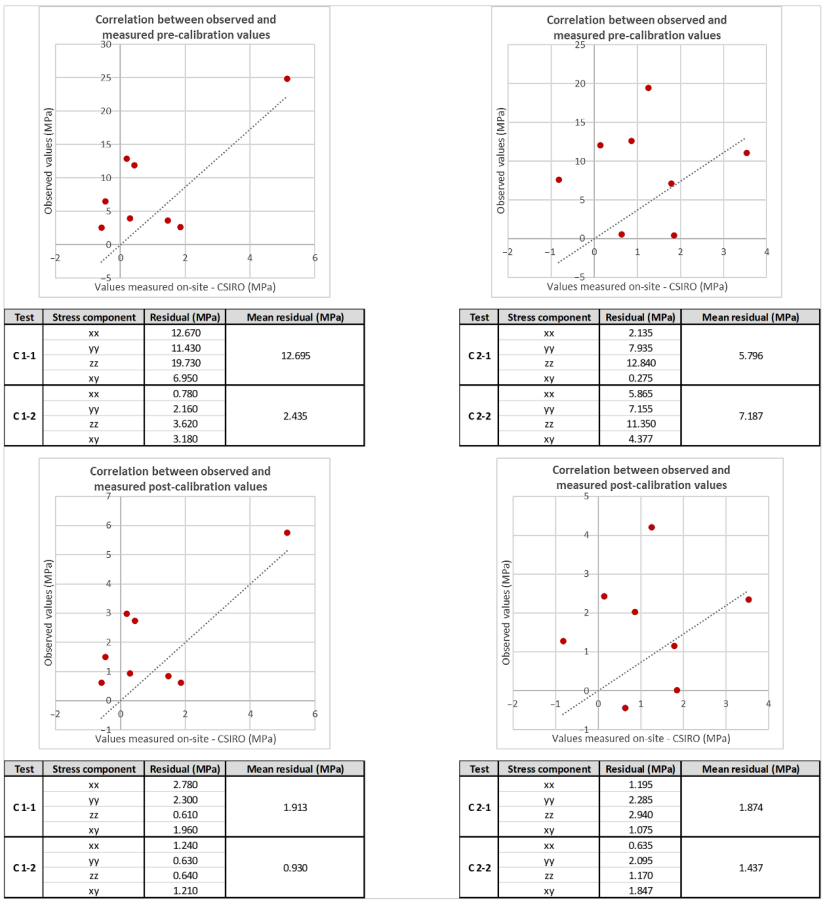

Test	Stress component	Residual (MPa)	Mean residual (MPa)
C 1-1	xx	12.670	12.695
	yy	11.430	
	zz	19.730	
	xy	6.950	
C 1-2	xx	0.780	2.435
	yy	2.160	
	zz	3.620	
	xy	3.180	

Test	Stress component	Residual (MPa)	Mean residual (MPa)
C 2-1	xx	2.135	5.796
	yy	7.935	
	zz	12.840	
	xy	0.275	
C 2-2	xx	5.865	7.187
	yy	7.155	
	zz	11.350	
	xy	4.377	

Test	Stress component	Residual (MPa)	Mean residual (MPa)
C 1-1	xx	2.780	1.913
	yy	2.300	
	zz	0.610	
	xy	1.960	
C 1-2	xx	1.240	0.930
	yy	0.630	
	zz	0.640	
	xy	1.210	

Test	Stress component	Residual (MPa)	Mean residual (MPa)
C 2-1	xx	1.195	1.874
	yy	2.285	
	zz	2.940	
	xy	1.075	
C 2-2	xx	0.635	1.437
	yy	2.095	
	zz	1.170	
	xy	1.847	

Figure 22. Correlation between the values observed in the CSIRO HI tests and those extracted from the model pre- and post-calibration in UDEC©.

Results from calibrated DEM modeling allowed us to localize tensile and compressive stresses along the two sections. The trend of the stress field around the quarry walls is shown in Figures 23 and 24, with information about the deviatoric stress and the main stresses σ_1 and σ_3 at the current condition of excavation. It must be pointed out that UDEC©, in a different way to RS3©, considers the negative sign as compression and the positive one as traction.

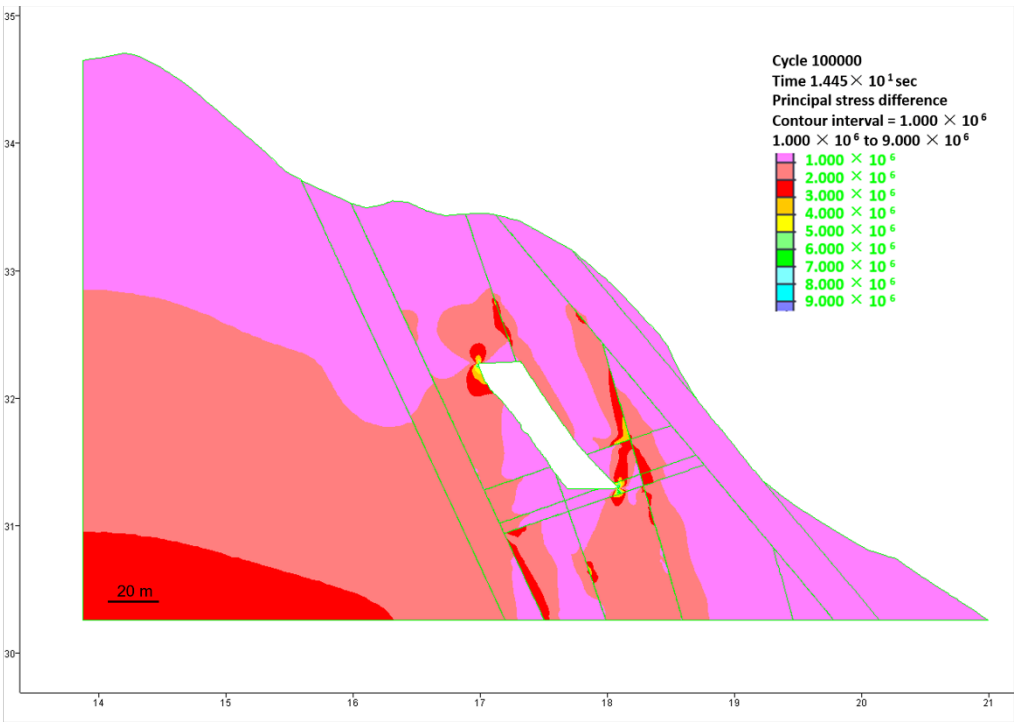

Figure 23. Deviatoric stress (σ_1–σ_3) of Section 1 calculated in Pa.

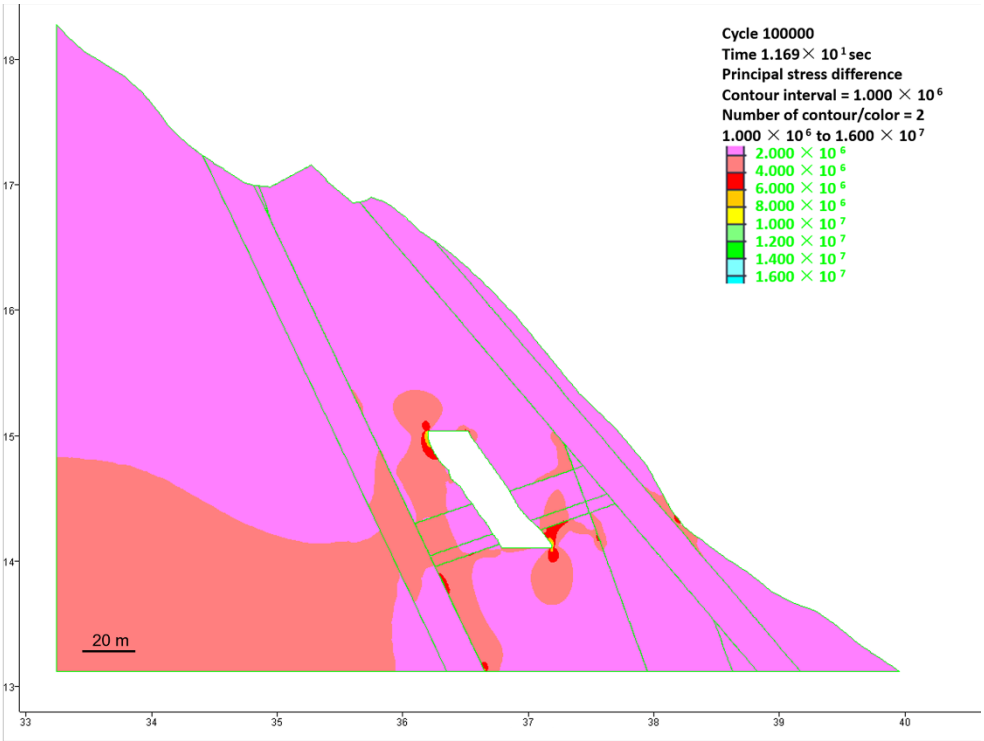

Figure 24. Deviatoric stress (σ_1–σ_3) of Section 2 calculated in Pa.

Using the calibrated 2D model, it was possible to simulate the next excavation step of the zone currently under marble exploitation. Figures 25 and 26, showing the deviatoric stresses as computed along S1 and S2, highlight the presence of high values in the acute edges of the quarry internal geometry up to 18 MPa. In the same zones, the maximum main stress σ_1 shows high compressive stresses, with values ranging from a minimum of −2 MPa to a maximum of 17 MPa, while σ_3 varies from a minimum value of −3 MPa to a maximum of 5 MPa.

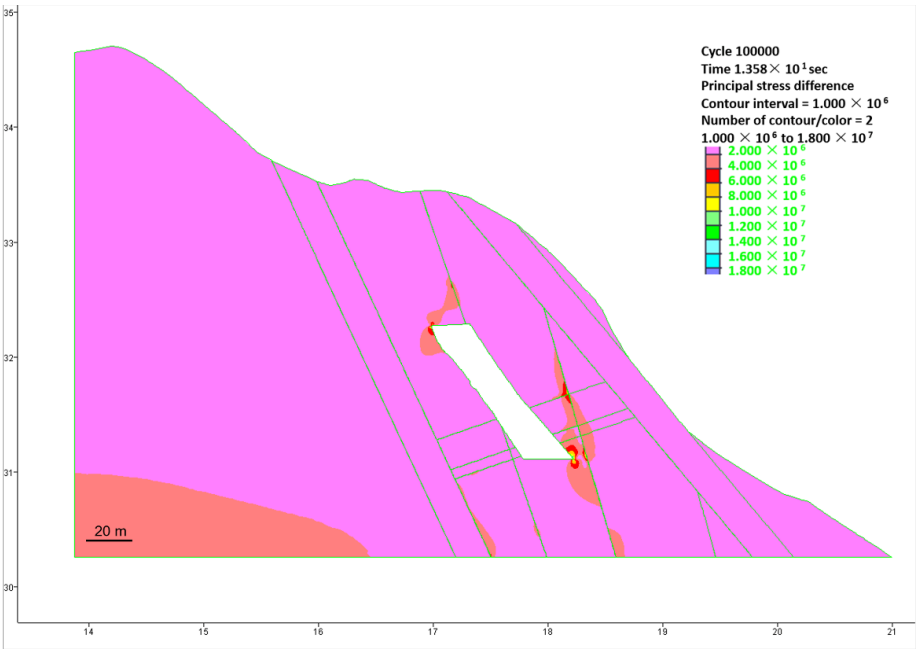

Figure 25. Deviatoric stress (σ_1−σ_3) of Section 1 calculated in Pa; the model includes the representation of future excavation.

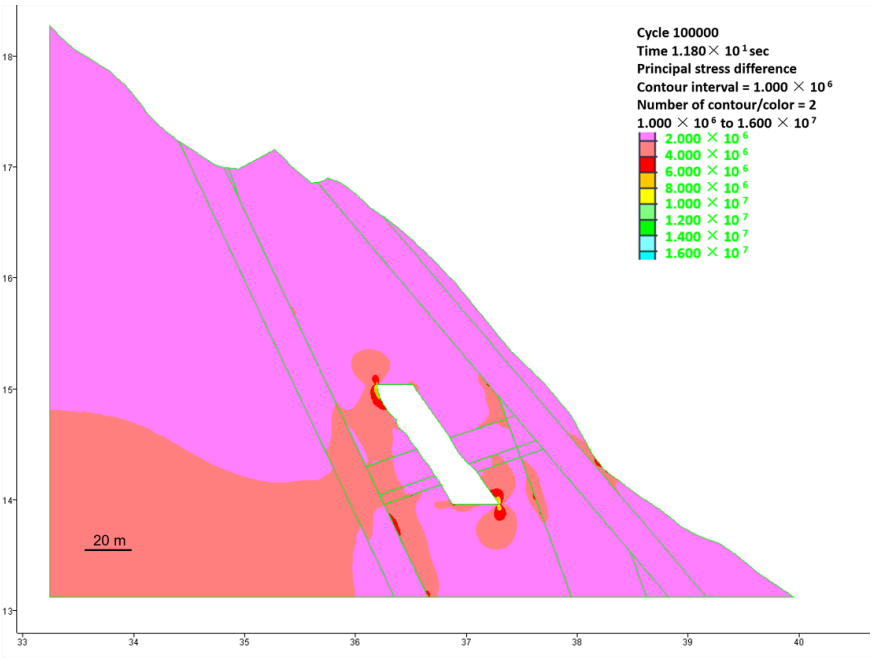

Figure 26. Deviatoric stress (σ_1−σ_3) of Section 2 calculated in Pa; the model includes the representation of future excavation.

5. Discussion

The CSIRO HI cell were used, in this paper, to calibrate the FEM and DEM numerical models with the aim of monitoring the in situ stress and the slope stability. This test is nowadays practiced quite often in several extraction sites of the Apuan Alps. One of the first studies published in this area by Gullì et al. [72] describes an experimental stress analysis that was applied in different Carrara marble underground quarries.

Referring to the same area, other papers illustrate slope stability numerical modeling without the use of in situ stress measurements, and they validate the results by back-analyses based on either past or recent evidence. Some of them use the DEM approach [12,73–76], and other ones use the FEM [64]. Pierotti et al. [77] adopted both FEM and DEM and validated their results in respect to those reported in [25]. The latter based its numerical modeling, DEM, and BEM (boundary element method, [78]), on data from in situ CSIRO HI cell tests. Similarly, several publications document the use of the overcoring method to validate the numerical models in the marble district of the Apuan Alps [25,26,65,79–81]. Mainly, they assess the reliability of models through a sensitivity analysis of the involved geomechanical parameters and through a comparison between the measured stresses and those numerically calculated. For example, Berlinghieri and Pandolfi [80] vary the lateral tension field K_0 with the goal of estimating the most realistic stress values backward given the measuring performed on-site.

In the present paper, an approach similar to that described in [82] was adopted. In Guido et al. [82], the FEM modeling was calibrated by means of a reiterate procedure of stress state data derived from 2D doorstopper tests. In our work, FEM and DEM numerical models were calibrated thanks to a similar procedure, written using the MATLAB© language, which provides a MLRA of a system of overdetermined equations. The obtained calibration has shown excellent results, with high values of Ra and very low deviations between the measured stresses and those numerically calculated.

The obtained results at the Sottovettolina quarry underline a high variability of tensional states, as identified both in the three-dimensional and two-dimensional modeling. It is noted that the highest values concerning the deviatoric stress, the maximum main stresses σ_1, and the minimum σ_3 are concentrated in restricted areas in all the presented models, located in the sharp and obtuse angle edges of the internal section of the quarry. According to [83] either external or internal angles with an assumed radius of curvature equal to zero (the so-called "angle point singularity") may show stress values which are theoretically infinite. Considering that this effect is limited to small areas, the Saint-Venant principle states that the effect of a load on a point is purely local and the stress due to this load decreases rapidly with the distance [84–86]. In this sense, the model can be improved by excluding the highly restricted areas by editing the shape of the edges, making them smoother. Table 6 shows the maximum and minimum values of σ_1, σ_3, and deviatoric stresses, both in the current state and in the forecasting one, after this exclusion phase.

Table 6. Values of σ_1, σ_3, and deviatoric stress (σ_1–σ_3) from FEM in agreement with the Saint-Venant principle and excluding the highly restricted areas affected by angle point singularity.

		Current Status	Future Excavation Scenario
$\sigma_1 - \sigma_3$ (MPa)		17	18
σ_1 (MPa)	Max	20	14
	Min	−2	−2
σ_3 (MPa)	Max	2	3
	Min	−9	−9

Analogous results come from the DEM modeling along S1 and S2 sections with high variability of tensional states near to the quarry angles. In particular, areas with acute edges show compressive stresses, while the obtuse edges of the quarry are affected by traction (Figure 27).

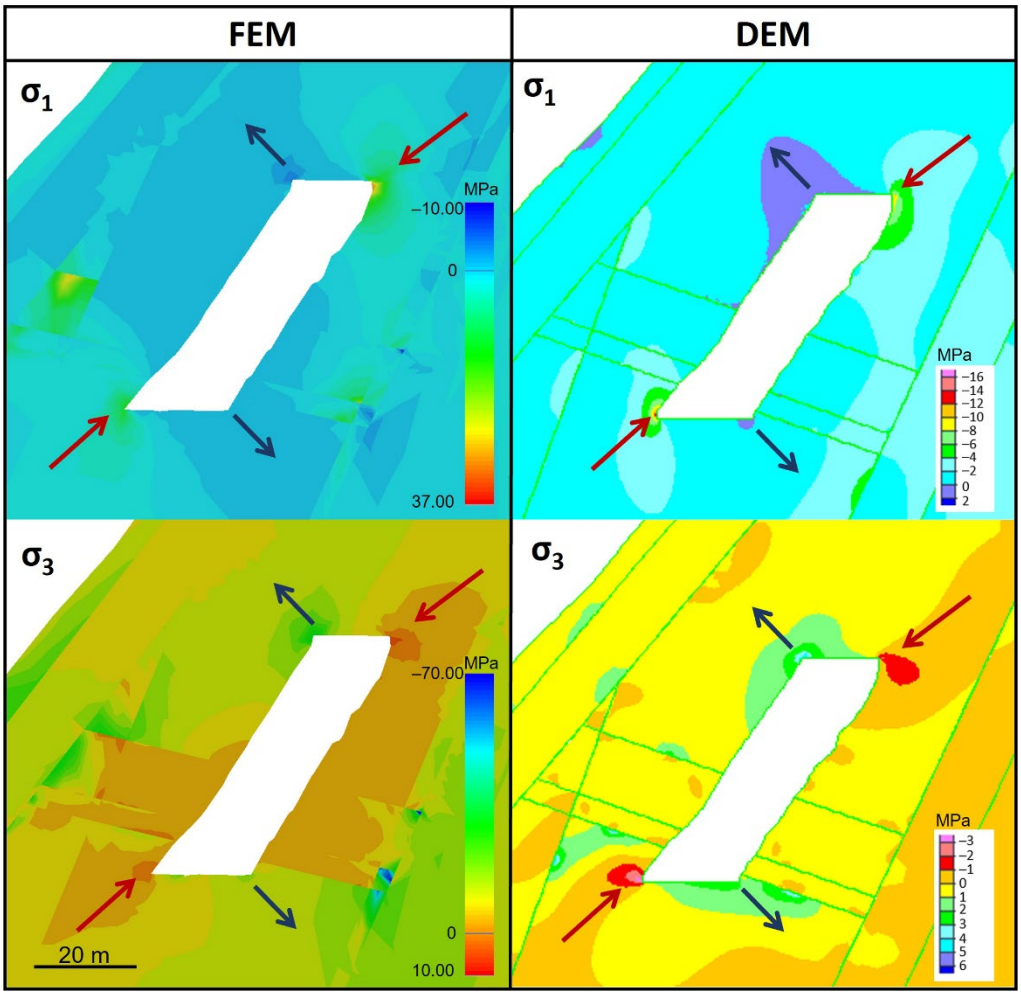

Figure 27. Comparison of stress values from FEM (RS3©) and DEM (UDEC©) models along the S2 section. The arrows show compressive stress (red) and tensile stress (blue), respectively. Note that DEM considers the negative sign as compression and the positive one as tensile stress, unlike the FEM model. The color scalebars, indicating the values of the in situ stresses in MPa, are created to compare zones of compressive and tensile stresses of the two models as best as possible.

In the proximity of the quarry, traction values show a general trend between −2 and −3 MPa, which are lower than both the tensile strength limit of −3.43 MPa, which is derived from geotechnical characterization of the quarry [47], and that proposed by [65] for the Carrara marbles which is set to -8 ± 3 MPa. Compressive stresses show maximum values of about 20 MPa which is lower than the compressive strength of the rock proposed by [47] and [65] and calculated to be 120 MPa and 100 ± 20 MPa, respectively.

The Hoek and Brown criterion [87] was used to critically evaluate the deviatoric stress resulting from the modeling. The criterion states the following:

$$\sigma_1 = \sigma_3 + \sqrt{(m \cdot \sigma_c \cdot \sigma_3 + s \cdot \sigma_c^2)} \quad (5)$$

where σ_c is the uniaxial compressive strength of the rock material, while m and s are, respectively, two empirical constants which depend on the internal friction angle of the rock mass and on the cohesion.

According to [88] a slightly fractured rock mass undergoes new failures when the deviatoric stress $\sigma_1 - \sigma_3$ exceeds the Hoek and Brown criterion. Setting the strength parame-

ters for the brittle failure criterion $m = 0$ and $s = 0.11$, the Hoek and Brown failure criterion becomes the following:

$$\sigma_1 - \sigma_3 = 0.33\ \sigma_c \quad (6)$$

Therefore, in the Sottovettolina quarry, considering an average σ_c equal to 100 MPa, the rock mass seems to undergo forcing where the following condition occurs:

$$\sigma_1 - \sigma_3\ \geq\ 0.33\ \cdot 100\ \text{MPa}\ = 33\ \text{MPa} \quad (7)$$

The deviatoric stress derived from the modeling is always below this threshold, and it shows a maximum value of 29 MPa in RS3© and 18 MPa in UDEC©.

If removing the highly restricted areas affected by angle point singularity and considering the Saint-Venant principle, the deviatoric stress of FEM reaches values close to 18 MPa (Table 6). According to [65], the strength parameters of the brittle failure criterion for the Carrara marble are set to $m = 0$ and $s = 0.04$, respectively. Therefore, the criterion relating the deviatoric stress to the compressive strength of the rock is computed as follows:

$$\sigma_1 - \sigma_3\ \geq\ 0.2\ \cdot 100\ \text{MPa}\ = 20\ \text{MPa} \quad (8)$$

Hence, the calculated deviatoric stress of FEM including future excavation activities is lower than the safety limit proposed by [65].

6. Conclusions

The present study describes the 2D and 3D numerical modeling at the Sottovettolina quarry, in the Apuan Alps marble district. The investigation method has been based on the following steps: (i) modeling of the internal and external geometry of the quarry through the use of TLS and aerial LiDAR surveys; (ii) estimation of the rock mass properties through engineering–geological surveys; (iii) in situ measurement of the stresses field through CSIRO HI cell tests using the overcoring method; (iv) 2D and 3D numerical modeling with calibration of the stress states; v) simulation of future excavation phases and evaluation of the slope stability and the related stress states.

Particular mention must be made of the advantages offered in this study by the CSIRO HI cell measurements that permitted us to minimize the errors and calibrate the models thanks to their accuracy and redundancy. A reiterate procedure was properly written using the MATLAB© language, and it allowed us to obtain very low deviations between the measured stresses and those which were numerically calculated.

We finally want to highlight the advantages of using LiDAR technology, when compared to the classical methodologies of surveying, as it permitted us a good geometric characterization (3D modeling) of the quarry's walls and its external areas.

It is possible to conclude that the integrated approach, based on geomatics, engineering–geological surveys, in situ measurement, and numerical modeling, allowed us to estimate the stress state in the quarry area in such a way as to provide a valid approach for detecting and monitoring the stress–strain behavior of the rocky walls, aimed at improving the site efficiency and safety. Future developments will involve the refinement of the present multi-methodological approach in the other quarries of the Apuan Alps.

Author Contributions: R.S. is the Unit Project Coordinator for the University of Siena; D.G. and D.M. coordinated research activities on behalf of the UOC Ingegneria Mineraria—USL Toscana Nord-Ovest, Tuscany Region; R.S., D.S., L.B., V.D.L. and A.R. carried out topographic surveys through GNSS, TS and TLS; R.S., L.B., V.D.L. and A.E. performed 3D modeling and rock slope stability analysis using RS3© and UDEC©; S.G. performed in situ stress tests using the CSIRO HI cells and data analysis. All the authors contributed to the text writing. All authors have read and agreed to the published version of the manuscript.

Funding: This research was funded by Tuscany Region through the UOC Ingegneria Mineraria—USL Toscana Nord-Ovest. Open Access Publication Grants of the University of Siena provided financial support for the dissemination of high-quality research content.

Institutional Review Board Statement: Not applicable.

Informed Consent Statement: Not applicable.

Data Availability Statement: Not applicable.

Acknowledgments: Authors appreciatively acknowledge the Land Information System and Planning Sector (SITA) of the Tuscany Region for providing LiDAR data. A special thank goes to the personnel of Marmi Ducale s.r.l. for their availability and assistance during fieldwork, and to Pandolfi, O., Berlinghieri, M., Sirgiovanni, E., and Vaselli, L. for their contribution to the research concerning rock mass characteristics.

Conflicts of Interest: The authors declare no conflict of interest.

References

1. He, K.; Li, Y.; Ma, G.; Hu, X.; Liu, B.; Ma, Z.; Xu, Z. Failure mode analysis of post-seismic rockfall in shattered mountains exemplified by detailed investigation and numerical modelling. *Landslides* **2021**, *18*, 425–446. [CrossRef]
2. Donati, D.; Stead, D.; Stewart, T.; Marsh, J. Numerical modelling of slope damage in large, slowly moving rockslides: Insights from the Downie Slide, British Columbia, Canada. *Eng. Geol.* **2020**, *273*, 105693. [CrossRef]
3. Donati, D.; Stead, D.; Brideau, M.; Ghirotti, M. Using pre-failure and post-failure remote sensing data to constrain the three-dimensional numerical model of a large rock slope failure. *Landslides* **2021**, *18*, 827–847. [CrossRef]
4. Guo, Y.; Li, X.; Ju, S.; Lyu, Q.; Liu, T. Utilization of 3D Laser Scanning for Stability Evaluation and Deformation Monitoring of Landslides. *J. Environ. Public Health* **2022**, *2022*, 8225322. [CrossRef] [PubMed]
5. Vanneschi, C.; Eyre, M.; Francioni, M.; Coggan, J. The use of Remote Sensing Techniques for monitoring and Characterization of Slope Instability. In *Procedia Engineering*; Elsevier Ltd.: Amsterdam, The Netherlands, 2017; Volume 191, pp. 150–157.
6. Cai, J.; Zhang, L.; Dong, J.; Dong, X.; Li, M.; Xu, Q.; Liao, M. Detection and characterization of slow-moving landslides in the 2017 Jiuzhaigou earthquake area by combining satellite SAR observations and airborne Lidar DSM. *Eng. Geol.* **2022**, *305*, 106730. [CrossRef]
7. Salvini, R.; Mastrorocco, G.; Esposito, G.; Di Bartolo, S.; Coggan, J.; Vanneschi, C. Use of a remotely piloted aircraft system for hazard assessment in a rocky mining area (Lucca, Italy), *Nat. Hazards Earth Syst. Sci.* **2018**, *18*, 287–302. [CrossRef]
8. Bar, N.; Kostadinovski, M.; Tucker, M.; Byng, G.; Rachmatullah, R.; Maldonado, A.; Pötschb, M.; Gaichb, A.; McQuillan, A.; Yacoubc, T. Rapid and robust slope failure appraisal using aerial photogrammetry and 3D slope stability models. *Int. J. Min. Sci. Technol.* **2020**, *30*, 651–658. [CrossRef]
9. Liu, C.; Liu, X.; Peng, X.; Wang, E.; Wang, S. Application of 3D-DDA integrated with unmanned aerial vehicle–laser scanner (UAV-LS) photogrammetry for stability analysis of a blocky rock mass slope. *Landslides* **2019**, *16*, 1645–1661. [CrossRef]
10. Salvini, R.; Riccucci, S.; Gullì, D.; Giovannini, R.; Vanneschi, C.; Francioni, M. Geological application of UAV photogrammetry and terrestrial laser scanning in marble quarrying (Apuan Alps, Italy). In *Engineering Geology for Society and Territory*; Springer: Cham, Switzerland, 2015; Volume 5, pp. 979–983.
11. Fuad, N.A.; Ismail, Z.; Majid, Z.; Darwin, N.; Ariff, M.F.M.; Idris, K.M.; Yusoff, A.R. Accuracy evaluation of digital terrain model based on different flying altitudes and conditional of terrain using UAV LiDAR technology. In *IOP Conference Series: Earth and Environmental Science*; IOP Publishing: Bristol, UK, 2018; Volume 169, p. 012100.
12. Francioni, M.; Salvini, R.; Stead, D.; Giovannini, R.; Riccucci, S.; Vanneschi, C.; Gullì, D. An integrated remote sensing-GIS approach for the analysis of an open pit in the Carrara marble district, Italy: Slope stability assessment through kinematic and numerical methods. *Comput. Geotech.* **2015**, *67*, 46–63. [CrossRef]
13. Francioni, M.; Salvini, R.; Stead, D.; Coggan, J. Improvements in the integration of remote sensing and rock slope modelling. *Nat. Hazards* **2019**, *90*, 975–1004. [CrossRef]
14. Huang, Y.H. *Slope Stability Analysis by the Limit Equilibrium Method*; American Society of Civil Engineers: Reston, VA, USA, 2014; pp. 1–365.
15. Cundall, P.A.; Strack, O.D.L. A Discrete Numerical Model for Granular Assemblies. *Geotechnique* **1979**, *29*, 47–65. [CrossRef]
16. Griffiths, D.V.; Lane, P.A. Slope stability analysis by finite elements. *Geotechnique* **1999**, *49*, 387–403. [CrossRef]
17. Kveldsvik, V.; Kaynia, A.M.; Nadim, F.; Bhasin, R.; Nilsen, B.; Einstein, H.H. Dynamic distinct-element analysis of the 800m high Åknes rock slope. *Int. J. Rock Mech. Min. Sci.* **2009**, *46*, 686–698. [CrossRef]
18. Alejano, L.; Ferrero, A.M.; Ramírez-Oyanguren, P.; Fernandez, M.A. Comparison of limit-equilibrium, numerical and physical models of wall slope stability. *Int. J. Rock Mech. Min.* **2011**, *48*, 16–26. [CrossRef]
19. Xu, B.; Liu, S.; Wang, J. An Analysis of Slope Stability Based on Finite Element Method and Distinct Element Method. In *Journal of Physics: Conference Series*; IOP Publishing: Bristol, UK, 2022; p. 2148.
20. Rocscience RS3: 3D Finite Element Analysis. Version 4.013. Available online: https://www.rocscience.com/help/rs3/ (accessed on 5 August 2022).
21. Bar, N.; McQuillan, A. 3D limit equilibrium slope stability analysis for anisotropic and faulted rock masses in Australian coal and iron ore mines. In Proceedings of the ISRM International Symposium-10th Asian Rock Mechanics Symposium, Singapore, 28 October–3 November 2018.

22. McQuillan, A.; Yacoub, T.; Bar, N.; Coli, N.; Leoni, L.; Rea, S.; Bu, J. Three-dimensional slope stability modelling and its interoperability with interferometric radar data to improve geotechnical design. In *Slope Stability 2020: Proceedings of the 2020 International Symposium on Slope Stability in Open Pit Mining and Civil Engineering*; Dight, P.M., Ed.; Australian Centre for Geomechanics: Perth, Australia, 2020; pp. 1349–1358.
23. Leeman, E.R. Rock stress measurements using the trepanning stress-relieving technique. *Mine Quarry Eng.* **1964**, *30*, 250–255.
24. Wortonincki, G. CSIRO triaxial stress measurement cell. In *Comprehensive Rock Engineering-Principles, Practice & Projects*; Hudson, J.A., Ed.; Pergamon: London, UK, 1993; Volume 3, pp. 329–394.
25. Ferrero, A.M.; Migliazza, M.; Segalini, A.; Gullì, D. In Situ stress measurements interpretations in large underground marble quarry by 3D modeling. *Int. J. Rock Mech. Min. Sci.* **2013**, *60*, 103–113. [CrossRef]
26. Gullì, D.; Pellegri, M.; Cortopassi, A. Experimental Approach for Stability Evaluations of Carrara Marble Basins. *Landslide Sci. Pract. Spat. Anal. Model.* **2013**, *3*, 211–217.
27. Ouanas, A.B.; Gunzburger, Y.; Lahaie, F.; Piguet, J.P.; Barnichon, J.D. Mechanical testing of hollow cores to determine elastic parameters of anisotropic rocks using the CSIRO HI cell. In *European Rock Mechanics Symposium 2010 (Eurock 2010)*; Zhao, J., Labiouse, V., Dudt., J.P., Mathier, J.F., Eds.; Taylor & Francis Group: London, UK, 2010; pp. 103–106.
28. Krietsch, H.; Gischig, V.; Jalali, M.R.; Amann, F.; Evans, K.F.; Doetsch, J.; Valley, B. Stress measurements in crystalline rock: Comparison of overcoring, hydraulic fracturing and induced seismicity results. In *51st US Rock Mechanics/Geomechanics Symposium*; ARMA, American Rock Mechanics Association: Alexandria, VA, USA, 2017; 8p.
29. Souley, M.; Renaud, V.; Al Heib, M.; Bouffier, C.; Lahaie, F.; Nyström, A. Numerical investigation of the development of the excavation damaged zone around a deep polymetallic ore mine. *Int. Jo. Rock. Mech. Min. Sci.* **2018**, *106*, 165–175. [CrossRef]
30. Adach-Pawelus, K.; Pawelus, D. Influence of Driving Direction on the Stability of a Group of Headings Located in a Field of High Horizontal Stresses in the Polish Underground Copper Mines. *Energies* **2021**, *14*, 5955. [CrossRef]
31. Dahnér, C.; Dineva, S. Small-scale variations in mining-induced stresses, monitored in a seismically active underground mine. In Proceedings of the Second International Conference on Underground Mining Technology, Perth, Australia, 3–4 November 2020; Australian Centre for Geomechanics: Perth, Australia, 2020; pp. 233–246.
32. Dight, P.M.; Snyman, L.A. Stress measurement for St Barbara Mines Gwalia Deeps project–one of the world's deepest underground haulage mines. *Min. Technol.* **2010**, *119*, 246–254. [CrossRef]
33. Amici, R.; Peach, G.; Nadeem, M. In-situ stress measurements in TBM tunnels prone to rockbursts. In *Tunnels and Underground Cities: Engineering and Innovation meet Archaeology, Architecture and Art*; CRC Press: Boca Raton, FL, USA, 2019; pp. 597–606.
34. Yang, J.; Chen, W.; Zhao, W.; Tan, X.; Tian, H.; Yang, D.; Ma, C. Geohazards of tunnel excavation in interbedded layers under high in situ stress. *Eng. Geol.* **2017**, *230*, 11–22. [CrossRef]
35. Borbély, D. Tunnel-excavation-induced permeability change of rock mass around a radioactive waste repository tunnel. *Cent. Eur. Geol. Cent. Eur. Geol.* **2018**, *61*, 73–84. [CrossRef]
36. Carmignani, L.; Kligfield, R. Crustal extension in the Northern Apennines: The transition from compression to extension in the Alpi Apuane core complex. *Tectonics* **1990**, *9*, 1275–1303. [CrossRef]
37. Molli, G. Northern Appennine–Corsica orogenic system: An updated review. In *Tectonic Aspects of the Alpine–Dinaride –Carpathian System*; Siegesmund, S., Fügenschuh, B., Froidzheim, N., Eds.; Geological Society of London Special Publication: London, UK, 2008; Volume 298, pp. 413–442.
38. Molli, G.; Vaselli, L. Structures, interference patterns and strain regime during mid-crustal deformation in the Alpi Apuane (Northern Appennines, Italy). In *Styles of Continental Contraction*; Special Papers; Mazzoli, S., Buler, R., Eds.; Geological Society of America: Boulder, CO, USA, 2006; Volume 414, pp. 79–93.
39. Molli, G.; Meccheri, M. Structural inheritance and style of reactivation at mid-crustal levels: A case study from the Alpi Apuane (Tuscany, Italy). *Tectonophysics* **2012**, *579*, 74–87. [CrossRef]
40. Carmignani, L.; Giglia, G.; Kligfield, R. Structural evolution of the Apuane Alps; an example of continental margin deformation in the northern Apennines, Italy. *J. Geol.* **1978**, *86*, 487–504. [CrossRef]
41. Molli, G. Deformation and fluid flow during underplating and exhumation of the Adria Continental margin: A one-day field trip in the Alpi Apuane (northern Apennines, Italy). In *Deformation, Fluid Flow and Mass Transfer in the Forearc of Convergent Margins: Field Guides to the Northern Apennines in Emilia and the Apuan Alps (Italy)*; Vannucchi, P., Fisher, D., Eds.; The Geological Society of America: Boulder, CO, USA, 2012; Volume 28, pp. 35–48.
42. Ottria, G.; Molli, G. Superimposed brittle structures in the late orogenic extension of the northern Apennine: Results from Carrara area (Alpi Apuane, NW Tuscany). *TerraNova* **2000**, *12*, 1–8. [CrossRef]
43. Molli, G.; Giorgetti, G.; Meccheri, M. Tectono-metamorphic evolution of the Alpi Apuane Metamorphic Complex: New data and constraints for geodynamic models. *Boll. Soc. Geol. It.* **2002**, *1*, 789–800.
44. Fellin, M.G.; Reiners, P.W.; Brandon, M.T.; Wuthrich, E.; Balestrieri, M.L.; Molli, G. Thermochronologic evidence of exhumational history of the Alpi Apuane metamorphic core complex, northern Appennines, Italy. *Tectonics* **2007**, *26*, 1–22. [CrossRef]
45. Kligfield, R.; Hunziker, J.; Dallmeyer, R.D.; Schamel, S. Dating of deformation phases using K-Ar and $^{40}Ar/^{39}Ar$ techniques: Results from the Northern Apennines. *J. Struct. Geol.* **1986**, *8*, 781–798. [CrossRef]
46. Carmignani, L.; Conti, P.; Fantozzi, P.L.; Mancini, S.; Massa, G.; Molli, G.; Vaselli, L. I marmi delle Alpi Apuane. *Geoitalia* **2007**, *21*, 19–30.
47. Pandolfi Engineering s.r.l. Relazione Tecnica–Caratterizzazione Geomeccanica del Versante. 2022; 24.
48. Barton, N.R. Review of a new shear strength criterion for rock joints. *Eng. Geol.* **1973**, *7*, 287–332. [CrossRef]

49. Deere, D.U.; Miller, R.P. *Engineering Classification and Index Properties for Intact Rock*; Technical Report AFNL-TR-65-116; Air Force Weapons Laboratory: Albuquerque, NM, USA, 1966; 277p.
50. Petrie, G.; Toth, K.C. Introducing to Laser Ranging, Profiling, and Scanning. In *Topographic Laser Ranging and Scanning. Principles and Processing*; Shan, J., Toth, K.C., Eds.; CRC Press: Boca Raton, FL, USA, 2008; pp. 1–27.
51. Voegtle, T.; Schwab, I.; Landes, T. Influences of different materials on the measurement of a Terrestrial Laser Scanner (TLS). In *Proceedings of the XXI Congress*; The International Society for Photogrammetry and Remote Sensing (ISPRS): Beijing, China, 2008; Volume XXXVII, pp. 1061–1066.
52. Pejić, M. Design and optimisation of laser scanning for tunnels geometry inspection. *Tunn. Undergr. Space Technol.* **2013**, *37*, 199–206. [CrossRef]
53. Vanneschi, C.; Salvini, R.; Massa, G. Geological 3D modeling for excavation activity in an underground marble quarry in the Apuan Alps (Italy). *Comput. Geosci.* **2014**, *69*, 41–54. [CrossRef]
54. Bertacchini, E.; Boni, E.; Capitani, A.; Capra, A.; Castagnetti, C.; Corsini, A.; Dubbini, M.; Parmeggiani, E. Stazione totale per il monitoraggio Leica TM30: Test di verifica secondo norme DIN-18723 e test di funzionamento per il monitoraggio frane. In Proceedings of the National Conference Asita 2009, Bari, Italy, 1–4 December 2009.
55. Beshr, A.A.A.; Elnaga, I.M.A. Investigating the accuracy of digital levels and reflectorless total stations for purposes of geodetic engineering. *Alex. Eng. J.* **2011**, *50*, 399–405. [CrossRef]
56. Hill, C.D.; Sippel, K.D. Modern Deformation Monitoring: A Multi Sensor Approach. In Proceedings of the XXII FIG International Congress, Washington, DC, USA, 19–26 April 2002.
57. Kirschner, H.; Stempfhuber, W. The Kinematic Potential of Modern Tracking Total Stations-A State of the Art Report on the Leica TPS1200+. In Proceedings of the 1st International Conference on Machine Control & Guidance, Zurich, Switzerland, 24–26 June 2008.
58. Kontogianni, V.; Kornarou, S.; Stiros, S. Monitoring with electronic total stations: Performance and accuracy of prismatic and non-prismatic reflectors. *Geotech. News* **2007**, *25*, 30–33.
59. Ganić, A.; Milutinović, A.; Tokalić, R.; Ognjanović, S. Measuring methods for cross sections of underground mine chambers. *Undergr. Min. Eng.* **2011**, *19*, 101–108.
60. Ask, D. Measurement-related uncertainties in overcoring data at the Äspö HRL, Sweden. Part 2: Biaxial tests of CSIRO HI overcore samples. *Int. Jo. Rock. Mech. Min. Sci.* **2006**, *43*, 127–138. [CrossRef]
61. Walton, R.J. *Hollow Inclusion (HI) Cell. Temperature Response and Correction*; Internal Document; Top Rock Technologies: Beaumaris, Victoria, Australia, 2012; 13p.
62. Amadei, B. *Rock Anisotropy and the Theory of Stress Measurement*; Springer: Berlin, Germany, 1983.
63. Amadei, B. *Analysis of Data Obtained with the CSIRO Cell in Anisotropic Rock Masses*; Technical Report N. 141; CSIRO Division of Geomechanics: Mt. Waverley, VIC, Australia, 1986.
64. Vanneschi, C.; Mastrorocco, G.; Salvini, R. Assessment of a Rock Pillar Failure by Using Change Detection Analysis and FEM Modelling. *ISPRS Int. J. Geo-Inf.* **2021**, *10*, 774. [CrossRef]
65. Gullì, D.; Pellegri, M.; Marchetti, D. Mechanical behaviour of Carrara marble rock mass related to geo-structural conditions and in-situ stress. In Proceedings of the Integrating Innovation of Rock Mechanics, 8th South American Congress on Rock Mechanics, Buenos Aires, Argentina, 15–18 November 2015.
66. Coulomb, C.A. Essai sur une application des regles des maximis et minimis a quelquels problemesde statique relatifs, a la architecture. *Mem. Acad. R. Div. Sav.* **1776**, *7*, 343–387.
67. Jiao, Y.; Zhao, J.; Ge, X. New formulation and validation of the three-dimensional extension of a static relaxation method. *Adv. Eng. Softw.* **2004**, *35*, 317–323. [CrossRef]
68. Cundall, P.A. A computer model for simulating progressive largescale movements in blocky rock systems. *Proc. Symp. Int. Soc. Rock Mech.* **1971**, *2*, 8.
69. Hart, R.D. An introduction to distinct element modelling for rock engineering. In *Charles Fairhurst Analysis and Design Methods*; Pergamon Press: Oxford, UK, 1993; pp. 245–261.
70. Cundall, P.A.; Hart, R.D. Numerical modelling of discontinua. In *Charles Fairhurst Analysis and Design Methods*; Pergamon: Oxford, UK, 1993; pp. 231–243.
71. Itasca. *UDEC User's Guide (Version 6.0)*; Itasca Consulting Group Inc.: Minneapolis, MN, USA, 2014.
72. Gullì, D.; Pellegri, M.; Cortopassi, A. Experimental study for stress analysis on different Carrara marble underground quarries. In Proceedings of the International Symposium on Deformation Characteristics of Geomaterials, Seoul, Korea, 1–3 September 2010; pp. 1296–1302.
73. Perazzelli, P.; Graziani, A.; Rotonda, T. Stability analysis of an active marble quarry by DEM modelling. In Proceedings of the International Conference on Rock Joints and Jointed Rock Masses, Tucson, AZ, USA, 7–8 January 2009; p. 1035.
74. Firpo, G.; Salvini, R.; Francioni, M.; Ranjith, P.G. Use of Digital Terrestrial Photogrammetry in rocky slope stability analysis by Distinct Elements Numerical Methods. *Int. Jo. Rock. Mech. Min. Sci.* **2011**, *48*, 1045–1054. [CrossRef]
75. Francioni, M.; Salvini, R.; Stead, D.; Litrico, S. A case study integrating remote sensing and distinct element analysis to quarry slope stability assessment in the Monte Altissimo area, Italy. *Eng. Geol.* **2014**, *183*, 290–302. [CrossRef]

76. Salvini, R.; Vanneschi, C.; Garattoni, A. Modellazione Stocastica Della Fratturazione (Metodo Discrete Fracture Network) a Supporto Della Stima Previsionale di Resa All'interno di Bacini Estrattivi di Pietre Ornamentali. Geologia Tecnica e Ambientale, 03-2020: 29-46. Available online: http://www.cngeologi.it/wp-content/uploads/2020/12/GTA03-2020low.pdf (accessed on 5 August 2022).
77. Pierotti, A.; Leoni, M.; Lo Presti, D. 3D FEM and DEM Analyses of Underground Openings in Competent Rock Masses. *Adv. Civil. Eng. Tech* **2020**, *4*, 10p.
78. Curran, J.; Corkum, B. *Examine3D*; User's guide; Rocscience: Toronto, ON, Canada, 2000.
79. Gullì, D.; Pellegri, M. Stress analysis on Carrara marble quarries. In Proceedings of the 6th International Symposium on In-Situ Rock Stress, Sendai, Japan, 20–22 August 2013; p. 17.
80. Berlinghieri, M.; Pandolfi, O. Three-dimensional Distinct Element Method for stability analysis of marble quarries in the Apuan Alps (Italy). *IOP Conf. Ser. Earth Environ. Sci.* **2021**, *833*, 8. [CrossRef]
81. Berlinghieri, M. Modellazione numerica al discontinuo per la coltivazione sotterranea di pietre ornamentali. In *Atti del X Incontro Annuale dei Giovani Ingegneri Geotecnici, Associazione Geotecnica Italiana, Roma, Italia*; Ceccato, F., Rosone, M., Stacul, S., Eds.; Associazione Geotecnica Italiana: Rome, Italy, 2021; pp. 27–30.
82. Guido, S.; Acerbis, R.; Sossi, G. Practice of the Doorstopper stress measurement method during the last 30 years in Italy. *IOP Conf. Ser. Earth Environ. Sci.* **2021**, *833*, 11. [CrossRef]
83. Bažant, Z.P.; Estenssoro, L.F. Surface singularity and crack propagation. *Int. J. Solids Struct.* **1979**, *15*, 405–426. [CrossRef]
84. Toupin, R.A. Saint-Venant's Principle. *Arch. Ration. Mech. Anal.* **1965**, *18*, 83–96. [CrossRef]
85. Horgan, C.O. Recent developments concerning Saint Venant's principle: An update. *Appl. Mech. Rev.* **1989**, *42*, 295–303. [CrossRef]
86. Nakamura, S.; Lakes, R. Finite element analysis of Saint-Venant end effects in micropolar elastic solids. *Eng. Comput.* **1995**, *12*, 571–587. [CrossRef]
87. Hock, E.; Brown, E.T. *Underground Excavations in Rock*; The Institution of Mining and Metallurgy: London, UK, 1980; 527p.
88. Martin, C.D.; Kaiser, P.K.; McCreath, D.R. Hoek-Brown parameters for predicting the depth of brittle failure around tunnels. *Can. Geotech. J.* **1999**, *36*, 136–151. [CrossRef]